DIPARTIMENTO DI MECCANICA

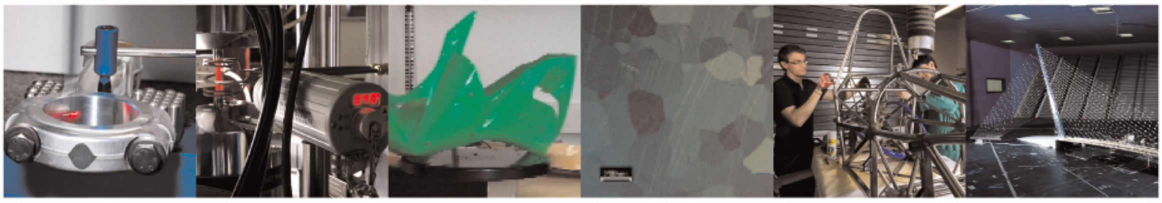

New Hot Workability Prediction Method under Non-Constant Deformation Conditions

Guo S.;Liu C.;Liang S.;Barella S.;Peng Y.;Gruttadauria A.;Belfi M.;Ouyang S.;Li D.;Karimi H. R.;Mapelli C.

DIPARTIMENTO DI MECCANICA ■ POLITECNICO DI MILANO
via G. La Masa, 1 ■ 20156 Milano ■ EMAIL (PEC): pecmecc@cert.polimi.it
http://www.mecc.polimi.it
Rev. 0

New Hot Workability Prediction Method under Non-Constant Deformation Conditions

Shuo Guo[a], Caiyi Liu[a*], Shicheng Liang[a], Silvia Barella[c], Yan Peng[a, b*], Andrea Gruttadauria[c], Marco Belfi[c], Sha Ouyang[d], De Li[b], Hamid Reza Karimi[c], Carlo Mapelli[c]

[a] State Key Laboratory of Crane Technology, Yanshan University, Qinhuangdao, 066004, China

[b] National Engineering Research Center for Equipment and Technology of Cold Strip Rolling, Yanshan University, Qinhuangdao, 066004, China

[c] Department of Mechanical Engineering, Politecnico di Milano, Milano, 20156, Italy

[d] Department of Mechanical Engineering, University of New Hampshire, Durham, New Hampshire, 03824, USA

[*] Correspondence: pengyan@ysu.edu.cn; liucaiyi@ysu.edu.cn

Abstract: The deformation conditions of metallic materials constantly change during forming and manufacturing technology. The thermomechanical processing theory cannot be applied to non-constant deformation conditions. The hot workability is a manifestation of the deformation conditions that affect the microstructure. This paper proposes a new prediction method based on artificial intelligence, considering the combined effect of microstructure state and deformation conditions. The hot deformation experiments under constant and non-constant deformation conditions validate the proposed method. Dynamic variation in deformation conditions significantly affects the hot workability. The findings indicate that reasonable control of the dynamic variation in deformation conditions during thermomechanical processing is conducive to improving the hot workability, providing new ways for equipment upgrading and process parameter optimization of some thermal processing technologies.

Keywords: hot deformation; hot workability; microstructure evolution; constitutive model; artificial neural network model; non-constant deformation conditions.

1. Introduction

Thermomechanical processing is a vital forming and manufacturing technology for metallic material. The material is deformed at a specific strain rate and temperature. Complex microstructure changes, including Work hardening (WH), dynamic recrystallization (DRX), dynamic recovery (DRV), and grain growth (GG), can be expected [1]. The microstructure evolution can effectively inhibit the formation of defects during deformation, improve the original microstructure, and reduce the deformation resistance [2]. However, microstructure changes are susceptible to deformation conditions [3]. Deformation degree, strain rate, and temperature changes affect the deformation mechanism and hot workability. Therefore, establishing a quantitative relationship between deformation conditions and hot workability is critical to manufacturing.

The thermomechanical processing map is a powerful tool to reflect the relationship between deformation conditions and hot workability. It is based on the superposition of the power dissipation rate η and instability parameter ξ. The two essential parameters are functions of strain, strain rate, and deformation temperature under dynamic material modeling theory. Generally, a high η associated with the dynamic softening process denotes good hot workability. Long et al. analyzed the η of magnesium alloy ZK61 under different deformation conditions and determined that the optimal hot workability can be obtained at 0.001-0.01s^{-1} and 623-673K [7]. Ding et al. investigated the hot workability of the extruded state magnesium alloy AZ31 under different deformation conditions. By analyzing the η, the optimum hot working process parameters were determined to be 0.005-0.05s^{-1} and 280-450°C. A higher DRX fraction was obtained at this process condition [8]. However, some cases with high η can also experience forming instability, including wedge cracks and pore instability [9]. The η is insufficient to fully reflect hot workability. Therefore, a comprehensive assessment in combination with the ξ is required. Wang et al. constructed hot processing maps of Ni alloys in the regions of 0.001s^{-1}-1s^{-1} and 980°C-1130°C. They demonstrated that shear deformation bands and microcracks formation at low temperatures and high strain rates caused deformation instability. The occurrence of DRX at high temperatures and low strain rates improved the hot workability [10]. Zhao et al. constructed hot processing maps of Ti-Al alloys under powder metallurgy and cast state in the regions of 700°C-1100°C and 0.001s^{-1}-10s^{-1}. They proved that the adiabatic shear bands, microcracks and flow localization caused hot workability deterioration [11]. Nayan et al. investigated hot processing maps of the Ni-Cu alloys in the regions of 0.01s^{-1}-10s^{-1} and 900°C-1200°C. The occurrence of stable deformation was associated with sufficient dynamic softening phenomena [12]. To optimize the forming conditions, Rajput et al. constructed hot processing maps of low carbon steels at 750°C-1050°C and 0.01-20 s^{-1}[13]. In summary, hot processing maps have been applied to various materials and deformation conditions. However, the application is all based on the assumption of constant deformation conditions, which change in a complex behavior in the actual process. The deformation is constantly undergoing transient variations, such as rolling, forging, extrusion, or drawing [14]. To combine the theory and the forming and manufacturing of materials, Kim et al. constructed hot processing maps to control the surface defects after hot bar rolling. He optimized the rolling process by superimposing deformation condition histories and hot processing maps while neglecting the effect of deformation conditions variations [15]. Sun et al. established the relationship between the η, ξ, and strain under the assumption of constant conditions by embedding the hot processing maps into a finite element model (FEM) [16]. Aneta, Lin, and Fuh et al. optimized the forging process by applying the above FEM method [17–19]. Jeong et al. proposed a method that combines 3D hot processing maps and FEM. The deformation condition history of each element is extracted and overlaid with the maps to evaluates the hot workability [20]. However, all the above applications are based on the assumption of constant deformation conditions. This assumption is inconsistent with the actual conditions and neglects the change in the deformation conditions.

Macro-level continuous variation in deformation conditions can result in adaptive micro-level microstructure variations. The hot workability is related to the deformation conditions and the microstructure. The same deformation conditions acting on different microstructures tend to obtain different forming qualities. Hu et al. compared the hot workability of 7Mo-0.37N-Re super austenitic stainless steel in a solid solution and pre-deformation state. The introduction of dislocation in the pre-deformation state improved the hot workability under the same deformation conditions [21]. Wu et al. compared the hot processing maps of low-density steels with different Al element contents. The increase in Al content increased the thermal activation energy, inhibited the softening effect of the DRX, and weakened the hot workability [22]. Pierce et al. found that as-cast materials with coarse grains are more prone to instability during the forming process. Coarse grains provide fewer DRX nucleation sites, and the dynamic softening during deformation is inhibited [23]. Nie et al. found that the increase in the initial DRX fraction improved the hot workability. The microstructure is an explicit function of the final deformation degree, strain rate, and temperature under constant deformation conditions. Thus, the coupling effect of microstructure and deformation conditions can be neglected. The hot workability can be calculated from the deformation conditions alone [24]. However, non-constant deformation conditions induce simultaneous microstructure updating. Chen et al. found that the strain rate transient increase transforms the DRX mechanism in the Ni-30%Fe alloy [25]. Liu et al. found that the strain rate transient decrease promoted the DRX effect [26]. Wang et al. found that the strain rate transients changing caused complex evolution of the texture and the proportion of twin boundaries (TBs) in Ni alloys [27]. Wu et al. found that the strain rate transients decrease increased the plasticity of Ti alloys [28]. Chen et al. found that the strain rate transient changing changes the DRX mechanism, the DRX fraction, average grain size (AGS), and hardness after deformation [29]. The mutual coupling of deformation conditions and microstructural states jointly leads to complex changes in hot workability. Therefore, it is necessary to illustrate the relationship between transient variation deformation conditions, microstructure, and hot workability to assess forming quality under non-constant deformation conditions. Samantaray et al. analyzed the relationship between the dynamic softening and the η of the 316L austenitic stainless steel. The DRX fraction increase and AGS refinement accompanied the improvement in the η [30]. Li et al. found that the dynamic softening of 300M steel was suppressed at low temperatures and high strain rates. A continuous deterioration of hot workability accompanies the accumulation of dislocation [31]. Lu et al. found that the peak of the η coincides with the saturation of the DRX [32]. However, most existing studies focus only on the qualitative relationship between deformation conditions, microstructure, and hot workability. Variables such as the temperature, strain rate, DRX fraction, AGS, and dislocation density are strongly coupled with hot workability. Constructing the relationship between the above variables and hot workability is quite challenging.

Artificial intelligence has shown advantages in constructing strongly coupled complex relationships [33]. Chen et al. designed a back propagation (BP) neural network model and trained it based on the experimental data. The strain, strain rate, and temperature were used to predict flow stress and thermal activation energy [34]. Kumar et al. trained several machine learning models with experimental data under constant deformation conditions to predict the hot workability. The accuracy was verified by comparing the corresponding microstructures [35]. Wen et al constructed a BP neural network model combining with genetic algorithm (GA). The model provided good predictions of the stress-strain behavior under constant deformation conditions [36]. Wen et al. quantitatively characterized the strong coupling effects of deformation temperature, strain rate, strain, and precipitates on DRX dynamics by constructing an artificial neural network based on a GA. The model effectively predicted the DRX kinetics and AGS evolution characteristics [37]. Wessel et al. characterized the plastic anisotropy of DX56D deep-drawn steel in and out of the yield plane with high accuracy based on machine learning techniques [38]. Li et al. developed a unified deep-learning-based phase transformation model to predict the transformation during all feasible loading paths in the hot stamping process [39]. Therefore, it is feasible to construct a relationship between deformation conditions, microstructure, and hot workability using artificial intelligence.

In this study, the most central work is developing a model that assesses the hot workability under non-constant deformation conditions, with which the impact of changing deformation conditions on the hot workability is analyzed. The outline of this paper is as follows: Section 2 describes the hot compression, the EBSD experiments procedure, and the basic theory of the constitutive model used in this paper. The hot compression experiments include both constant and non-constant deformation conditions. The constitutive model, linking the deformation conditions and the microstructure states, is the crucial foundation of the hot workability prediction method. Section 3 describes the framework and establishment procedure of the hot workability prediction method. It is a neural network structure where the deformation conditions and the microstructure states are the input variables, and the hot workability is the output variable. In Section 4, the model is validated, and the correlation between deformation conditions, microstructure states, and hot workability is analyzed in conjunction with model calculations and characterization. The proposed prediction method can provide a new idea for assessing and optimizing hot workability in the manufacturing process of metallic materials.

2. Experiments and Methods

This section describes the experimental procedure and conditions, including the hot compression and EBSD characterization experiments. The hot compression experiments are conducted at the constant and non-constant conditions. The experimental data are used to validate the methodology proposed in this paper. Moreover, the basic constitutive model is described to construct the quantitative relationship between deformation conditions and microstructure states. It is the key foundation of the hot workability prediction method.

2.1 Experiment procedure and conditions

The Gleeble 3800-GTC thermo-mechanical physical simulation system is used to simulate thermomechanical processing conditions to obtain flow-stress characteristics. A hot rolled 316L austenitic stainless steel plate is superior selected as the test material. Since it hardly undergoes phase transformation during the cooling process, which makes it possible to more clearly convenient to characterize the microstructure during high temperature plastic deformation. The elemental compositions can be found in previous studies [40]. Fig. 1. (a) shows the experimental procedure. The cylindrical specimens (φ8×12 mm) are used for uniaxial compression tests. The specimens are first heated to 1150℃ at 10℃/s and maintained for 5 min to ensure temperature homogenization. The temperature is then reduced to the target deformation temperature at 5°C/s and held for 1 min to minimize the temperature difference. Then the specimens are deformed to 0.9 true strain at a set strain rate (physically simulate actual deformation speed transient mutations). After deformation the specimen is rapidly water quenching to maintain the microstructure morphology of high temperature transient mutations. The tests are categorized into constant and non-constant deformation condition tests. As shown in Fig. 1. (b), there are nine groups of constant deformation condition tests. The three deformation temperatures are 1000, 1050, and 1100°C. The three strain rates are 0.01, 0.1, and 1s^{-1}. Fig. 1. (c)-(d) shows the non-constant deformation conditions. First, the material is deformed to 0.4 true strain at constant deformation conditions. Subsequently, a dynamic change in strain rate occurs, and deformation continues to 0.9 true strain. Table. 1. shows six sets of experimental conditions. The first three sets undergo an increase in strain rate from 0.01-1s^{-1} at about 0.4 true strain. The strain intervals required for strain rate changes are 0 (transient change), 0.2, and 0.5, respectively. In contrast to the first three, the last three groups undergo a decrease in strain rate from 1-0.01 s^{-1}. As shown in Fig. 1. (c)-(d), the logarithm strain rate varies linearly over the specified strain interval.

After completing the above tests, the compressed specimens are cut along the axis. The EBSD characterization is carried out with a Zeiss Sigma 500 SEM (Scanning Electron Microscope) equipped with an Oxford C-Nano detector. It is applied to characterize the center of the section parallel to the compression direction. The cut surfaces are first polished. Then, the samples are electropolished with 10% perchloric acid and 90% acetic acid solution at room temperature. The voltage is 30V, the polishing time is 45-60s, and the corresponding current is 0.2-0.7A. The scanning step size is 0.6 microns. The characterization images counted the AGS and the DRX fraction.

Table. 1. Six sets of experiments with changing deformation conditions.

Type	Temperature (℃)	Strain Rate (s^{-1})	Changing Occur at	Strain Intervals

1	1000	From 0.01 to 1	0.4 true strain	0
2	1000	From 0.01 to 1	0.4 true strain	0.2
3	1000	From 0.01 to 1	0.4 true strain	0.5
4	1000	From 1 to 0.01	0.4 true strain	0
5	1000	From 1 to 0.01	0.4 true strain	0.2
6	1000	From 1 to 0.01	0.4 true strain	0.5

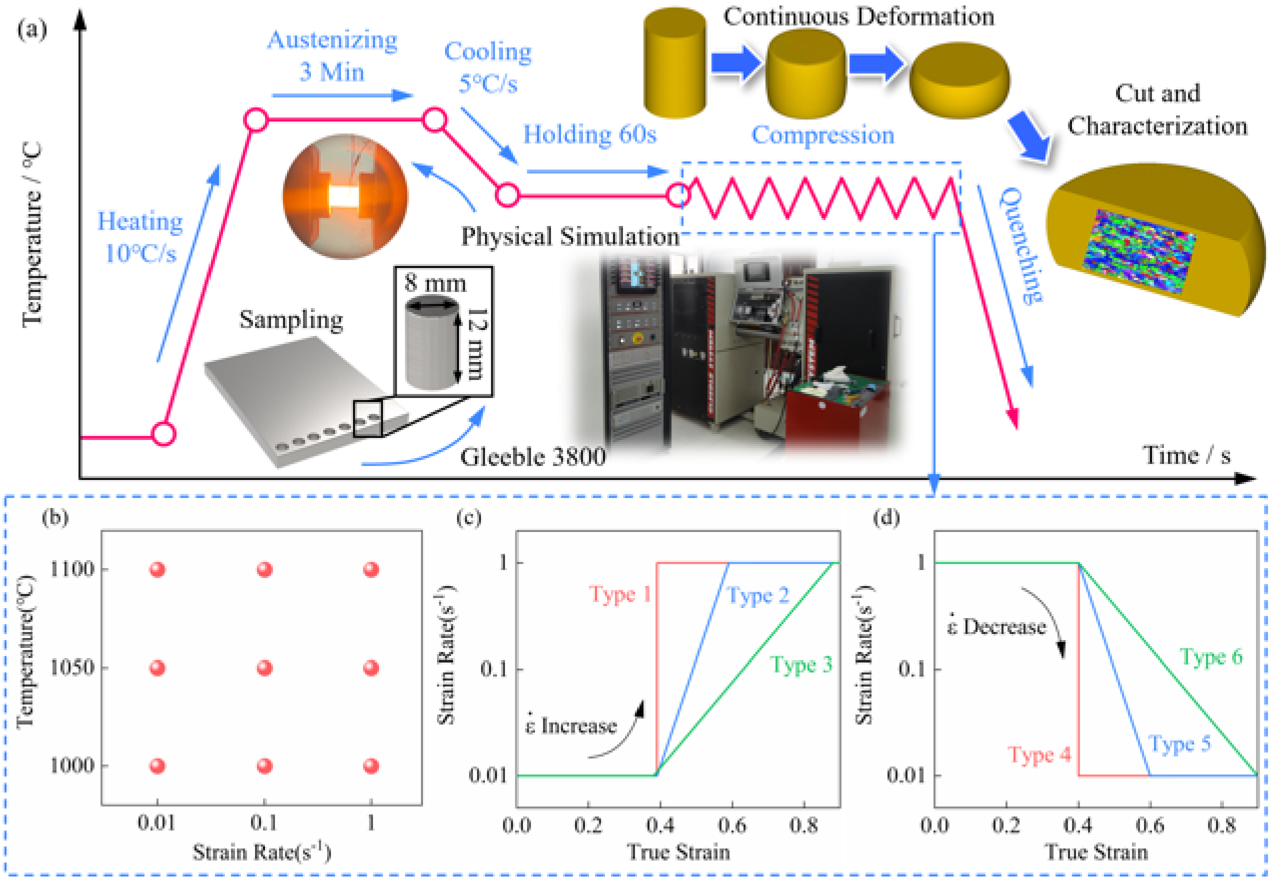

Fig. 1. (a) The experimental procedure of hot compression and characterization; (b) The experimental conditions for steady state deformation; (c) The experimental conditions for the case of strain rate increase; (d) The experimental conditions for the case of strain rate decrease.

2.2 The constitutive model using in the paper

In order to link the history of deformation conditions with the microstructure, this paper constructs a physically-based constitutive model with internal variables. The model considers the phenomena of the WH, DRV, DRX and GG during deformation [41]. The model can realize the coupled prediction of flow stress, DRX fraction, dislocation density and AGS. Eq. (1) are the constitutive model:

$$\begin{cases} \sigma_E = E\varepsilon_E \\ \sigma = \sigma_a + \sigma_{th} \\ \sigma_{th} = \dfrac{1}{A_2} arcsinh\left(\dfrac{\dot{\varepsilon}}{A_1}\right)\left(\dfrac{d}{d_0}\right)^{\gamma_1} + \sigma_0 \\ \dot{\sigma_a} = 0.5B\bar{\rho}^{-0.5}\dot{\bar{\rho}} \\ \dot{\bar{\rho}} = A_3\left(\dfrac{d}{d_0}\right)^{\gamma_2}(1-\bar{\rho})\dot{\varepsilon}^{\delta_1} - C\bar{\rho}^{\delta_2} - \dfrac{A_4\bar{\rho}}{(1-X_d)^{\delta_3}}\dot{S}\dot{\varepsilon}^{b_1} \\ \dot{X_d} = \bar{\rho}[\chi\varepsilon - \varepsilon_c(1-X_d)](1-X_d)^{\lambda}N \\ \dot{\chi} = A_5(1-\chi)\bar{\rho} \\ \dot{d} = A_6\left(\dfrac{d}{d_0}\right)^{\gamma_3} - A_7\dot{X_d}^{\gamma_5}\left(\dfrac{d_d}{d_0}\right)^{\gamma_4} \end{cases} \tag{1}$$

where σ_E is the stress in the elastic stage, and E is the elastic modulus. The plastic stress consists of two components [42]: thermally activated stress σ_{th} and non-thermal stress σ_a. The thermally activated stress denotes the initial slip resistance, which is related to the temperature, strain rate, and alloying elements. σ_0 is yield stress. The non-thermal stress σ_a characterizes the effect of the long-range obstacles on dislocation motion, which is related to the normalized dislocation density $\bar{\rho}$. $\dot{\bar{\rho}}$ is the normalized dislocation density change rate. $\dot{S}$ is the dynamic recrystallization rate, which considers the nucleation and growth process of the DRX. ε_c is the critical strain used to determine whether DRX has occurred. It is a function of temperature and strain rate. χ is the DRX incubation fraction, which indicates the incubation period required for the DRX. The AGS evolution considers two parts [43]: 1) the GG through grain boundary migration under the effect of thermal activation ($A_6\left(\frac{d}{d_0}\right)^{\gamma_3}$) and 2) the grain refinement under the effect of DRX ($A_6\left(\frac{d}{d_0}\right)^{\gamma_3}$). d_d represents the DRX grain size, which is a function of temperature and strain rate. A_3, C, and A_5, A_6, A_7 values are temperature dependent, as shown in Eq. (2). They consider the temperature effects on the WH, DRV, DRX and grain boundary migration ability [44]. The other coefficients in the model represent the material constants, fixed values not dependent on the change in deformation conditions. A specific explanation of the physical meaning can be found in previous papers [45].

$$\begin{cases} A_3 = A_{30}exp\left(\dfrac{Q_{A_3}}{RT}\right) \\ C = C_0 exp\left(-\dfrac{Q_C}{RT}\right) \\ A_5 = A_{50}exp\left(-\dfrac{Q_{A_5}}{RT}\right) \\ A_6 = A_{60}exp\left(-\dfrac{Q_{A_6}}{RT}\right) \\ A_7 = A_{70}exp\left(-\dfrac{Q_{A_7}}{RT}\right) \end{cases} \tag{2}$$

N represents the DRX nucleation rate. It is influenced by the temperature and strain rate:

$$N = N_0\dot{\varepsilon}^{b_2}exp\left(-\dfrac{Q_N}{RT}\right) \tag{3}$$

3. The Overall Framework and Construction Details

This section describes the overall framework and construction process of the proposed hot workability prediction method. It considers the effects of the microstructure states and deformation conditions. The dislocation density, DRX fraction, AGS, temperature, and strain rate are selected as inputs. Power dissipation rate and deformation instability factor measure the hot workability. The relationship between the input and output values is handled by the BP neural network model. It is trained based on experimental data under the constant deformation conditions (the hot workability can be calculated according to a fixed formula). Finally, the trained model can determine the hot workability under the non-constant deformation conditions based on the microstructure states and deformation conditions.

3.1 The overall framework

This paper proposes a BP neural network prediction method for hot workability. It takes into account the coupled effects of microstructure states and deformation conditions. The overall framework and construction process is shown in Fig. 2. The construction process is divided into three parts: 1) the construction of the constitutive model and hot processing maps; 2) the construction and training of the BP neural network; and 3) the validation and application of the BP neural network. Firstly, the flow stress, DRX fraction, and AGS changes are obtained based on the compression experiments and microstructure characterization. The specific parameters of the constitutive model (described in section 2.2) are solved by the GA. Moreover, the η and ξ under different deformation conditions are solved according to the basic theory of the hot processing maps. Secondly, a BP neural network coupling the effects of microstructure states and deformation conditions on hot workability is constructed and trained. The BP neural network is constructed by MATLAB software, which contains a three-layer structure: input, hidden, and output layers [36]. Eighty-one sets of experimental data for all constant deformation conditions are selected as the training set (three deformation temperatures, three strain rates, nine true strain). The constitutive model calculated the normalized dislocation density, DRX fraction, and AGS under the above deformation conditions. They are set as the microstructure state parameters. The deformation condition parameters are the current deformation temperature and strain rate. The above five parameters are used as input layer neurons and are normalized before input [46]. In addition, since the strain rate varies significantly, the strain rate is normalized after logarithms [47, 48].

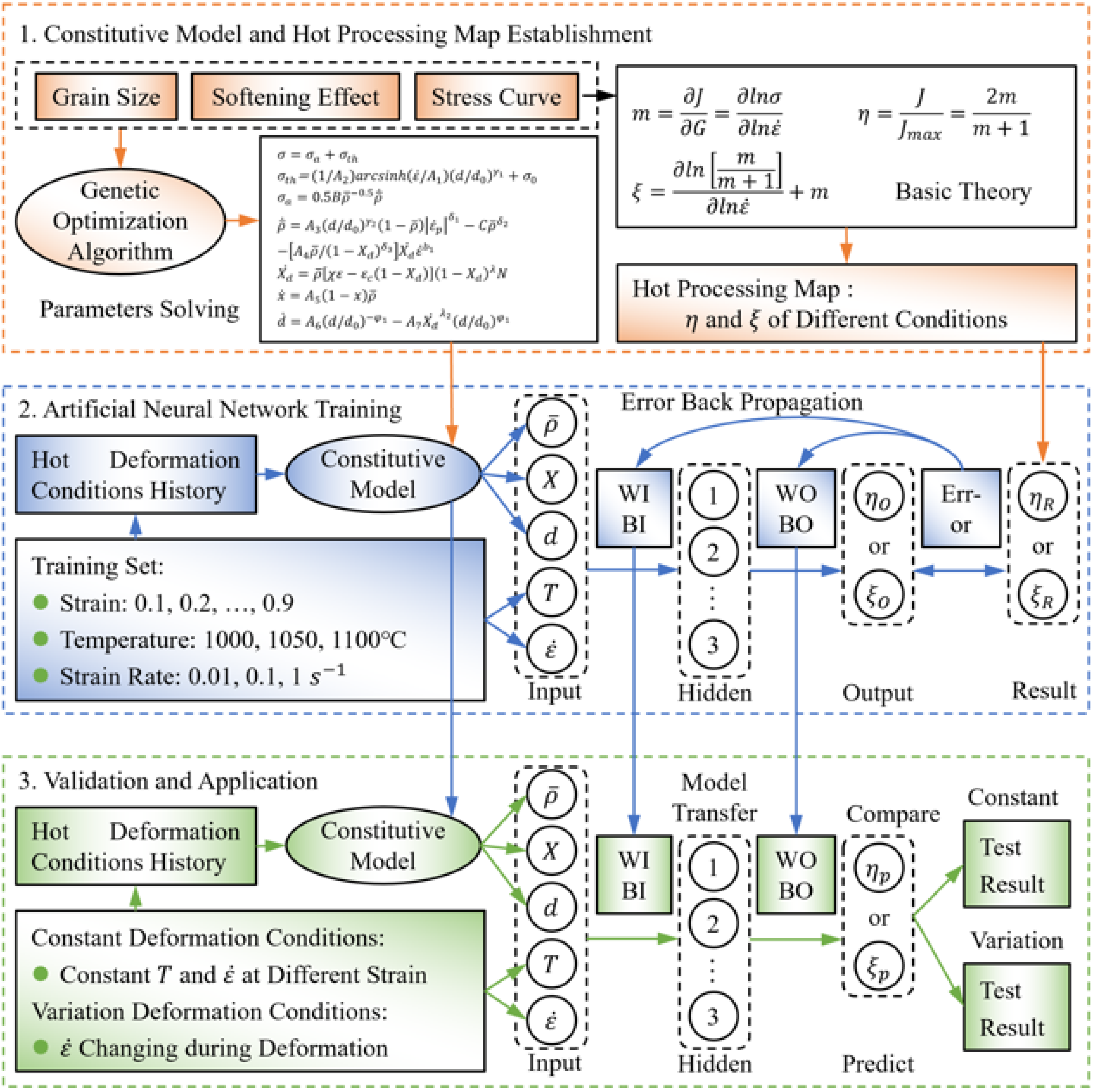

Fig. 2. A novel theoretical framework of the hot workability prediction method, including the constitutive model and hot processing maps establishment and the artificial neural network establishment, training, validation and application.

The hidden layer has a total of 6 neurons. The number of units in the hidden layer should be manageable to avoid overfitting or falling into the local optimal solution. There is only one neuron in the output layer. The hidden and output layer processes the input dislocation density, DRX fraction, AGS, deformation temperature, and strain rate to obtain the η or ξ. The processing method between different layers in the BP neural network can be found in the literature [34]. The activation functions between the input layer and the hidden layer and between the hidden layer and the output layer are chosen to be in Sigmod and Purelin forms, respectively [34].

The training process of the neural network is as follows: First, the program self-generates the weights and deviations between layers. Feedforward calculation is performed based on the parameters input from the training set. The error is obtained and feedbacked to correct the weights and deviations by comparing the calculated values with the experimental results. The above process is repeated until the error meets the requirements and retains the trained neural network structure. Finally, the trained neural network is verified and applied. The steady-state deformation conditions that are not in the training set are chosen to validate. The hot workability of the non-constant deformation experiments (described in section 2.1) is predicted. It is compared with the EBSD characterization results for illustration.

3.2 Parameters solution and validation of the constitutive model

The constitutive model parameters solution is characterized by multi-parameter and strong coupling, which is difficult to accomplish by direct fitting methods. Here, the solution steps are divided into three parts: 1) establishing the relationship between σ_0, ε_c, d_d and deformation conditions through Zener parameters; 2) solving the parameters related to the WH, DRV, and GG process by GA; and 3) solving the parameters related to the DRX process by GA [49].

The yield stress value was chosen as the corresponding stress at 0.02 true strain. The Jonas method determined the critical strain based on the inflexion point of the θ-σ curve, where the work-hardening rate is the derivative of stress to strain [50]. The DRX grain size was determined from characterization images. Finally, the Zener model unifies the relationship between deformation temperature, strain rate and characteristic parameters, as shown in Eq. (4)-(5) [46].

$$Z = \dot{\varepsilon} exp\left(-\frac{Q}{RT}\right) \tag{4}$$

$$\begin{cases} \sigma_0 = a_{\sigma_0} Z^{b_{\sigma_0}} \\ \varepsilon_c = a_{\varepsilon_c} Z^{b_{\varepsilon_c}} \\ d_d = a_{d_d} Z^{b_{d_d}} \end{cases} \tag{5}$$

Where Q is the thermal activation energy, R is the gas constant, which takes the value of 8.315, and a_{σ_0}, b_{σ_0}, a_{ε_c}, b_{ε_c}, a_{d_d}, and b_{d_d} are the fitting parameters for the σ_0, ε_c, and d_d. The activation energy can be found in previous studies [45]. The GA solves other model parameters, and the process is divided into two parts for convenience. Firstly, the flow stress before critical strain is used to solve the parameters related to the WH, DRV, and GG processes. Secondly, the flow stress, DRX fraction, and AGS of the whole process are used to solve the parameters related to the process of DRX. The GA in MATLAB software solved the model coefficients. The minimal residuals between the predicted and experimental data are the objective function [52]. The details of the solution process can be found in other literature. Table .2. shows the model coefficients.

Table. 2. The coefficients of the constitutive model.

Coefficient	Value	Coefficient	Value
$\boldsymbol{A_1}$	3.446893	A_4	5.00132
$\boldsymbol{A_2}$	0.266158	δ_3	0.94333
$\boldsymbol{B}$	127.0389	b_1	0.0012
$\boldsymbol{A_{30}}$	9.085×10^{-7}	λ	1.30021
$\boldsymbol{Q_{A_3}}$**(KJ/Mol)**	1837.2005	N_0	1739.668
$\boldsymbol{\delta_1}$	1.476997	b_2	0.0015
$\boldsymbol{C_0}$	10815.11	Q_N(KJ/Mol)	-1458.48
$\boldsymbol{Q_C}$**(KJ/Mol)**	-533.8197	A_{50}	2.35×10^{12}
$\boldsymbol{\delta_2}$	17.66317	Q_{A_5}(KJ/Mol)	-3501.18
$\boldsymbol{A_{60}}$	5.787×10^{7}	Q_{A_6}(KJ/Mol)	-2439.74
$\boldsymbol{A_{70}}$	268337.3	Q_{A_7}(KJ/Mol)	-1264.97
$\boldsymbol{a_{\sigma_0}}$	0.09889	b_{σ_0}	2.61028
$\boldsymbol{a_{\varepsilon_c}}$	0.00007458	b_{ε_c}	0.22846
$\boldsymbol{a_{d_d}}$	55615917	b_{d_d}	-0.48113
$\boldsymbol{\gamma_1}$	0.00693	γ_2	0.00174
$\boldsymbol{\gamma_3}$	-1.8873	γ_4	0.5742
$\boldsymbol{\gamma_5}$	0.5801		

Fig. 3. compares the predicted and experimental values of the flow stress, AGS, and DRX fraction for different strain rates and temperatures. The solid lines are the predicted values, and the dots are the experimental values. Fig. 3. (a) and(d) shows the flow stress curves at 1000°C with different strain rate and 0.01s^{-1} with different temperatures. The flow stresses under different deformation conditions are of two types: DRV (no significant softening stage) and DRX (significant softening followed by stabilization). The temperature and strain rate control the mechanism of microstructure evolution, which further determines the variation of flow stress [53, 54]. As shown in Fig. 3. (b) and (e), the DRX fraction is suppressed at low-temperature and high-strain-rate conditions. As a result, the flow stress is saturated and stabilized by the WH and DRV. The elevated temperature and reduced strain rate promote DRX behavior. Therefore, at 0.01 s^{-1}, the flow stress decreases and gradually approaches the steady state. In addition, the DRX has the effect of grain refinement. As shown in Fig. 3. (c) and (f), the AGS decreases gradually with the occurrence of DRX, and when the DRX reaches a certain level, the AGS enters a steady state. The effect of DRX on grain refinement

is more pronounced at low temperatures and high strain rates, although the DRX is inhibited. At 1000°C, the AGS at $0.1s^{-1}$ is smaller than that at $0.01s^{-1}$ and $0.01s^{-1}$. The smallest AGS is achieved at 1000°C compared to 1050°C and 1100°C. Low-temperature, high-strain-rate deformation conditions produced smaller DRX grain sizes. Moreover, the GG process is suppressed significantly. Notably, significant grain size growth occurred before and after DRX at 1050°C and 1100°C and a strain rate of 0.01 s^{-1}. High temperature and low strain rate give more grain boundary migration capacity and time to the origin and DRX grains.

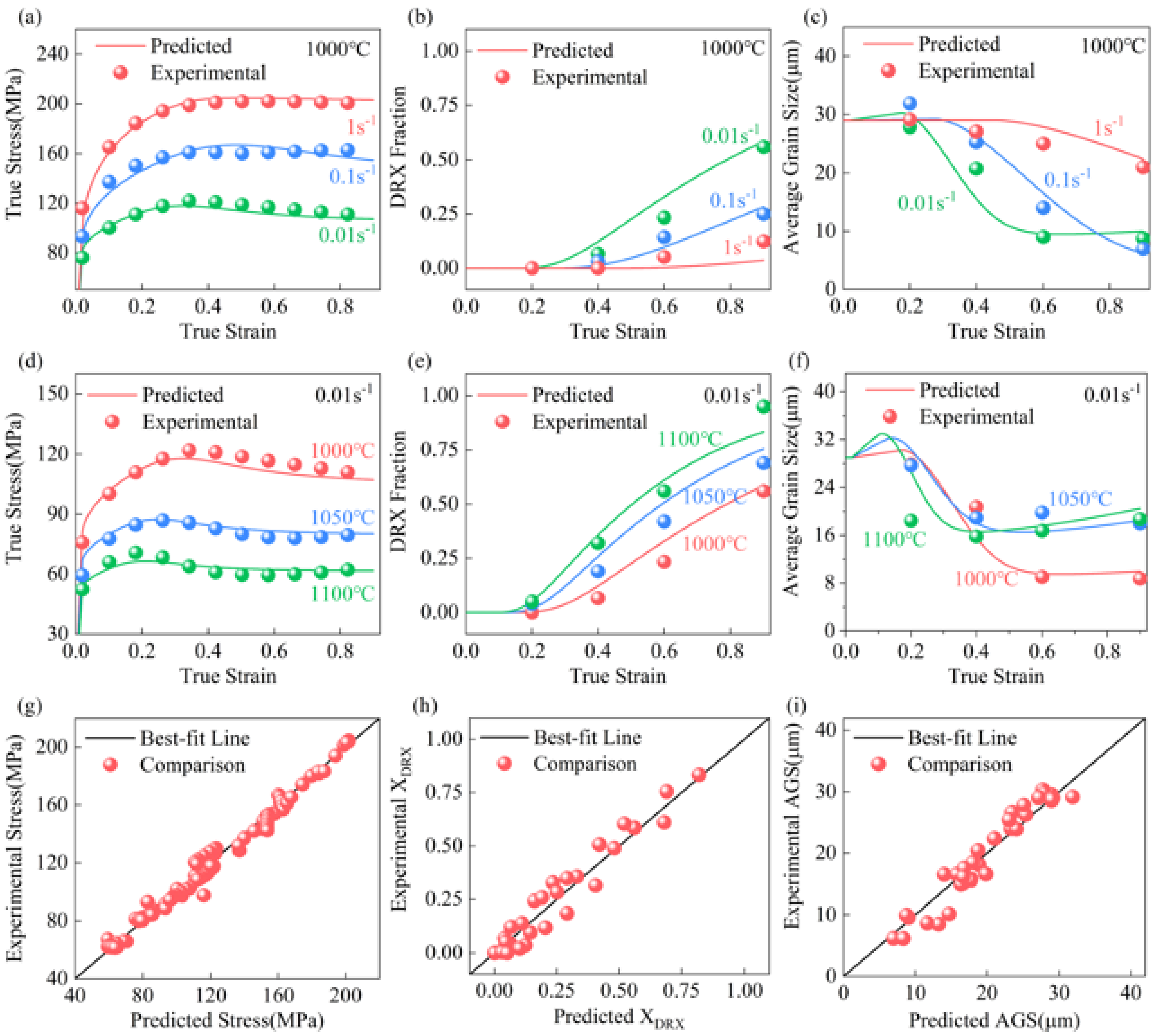

Fig. 3. The comparison of the predicted and experimental values for the flow stress, DRX fraction, and AGS, where different colors represent different deformation conditions, in (a)-(f), the solid lines are the predicted values and the solid dots are the experimental values: (a) Flow stress curves at different strain rates and 1000°C; (b) Flow stress curves at different temperatures and $0.01s^{-1}$; (c) DRX fraction curves at different strain rates and 1000°C; (d) DRX fraction curves at different temperatures and $0.01s^{-1}$; (e) AGS curves at different strain rates and 1000°C; (f) AGS

curves at different temperatures and $0.01s^{-1}$; in (g)-(i), the solid lines are the best fit line and the solid dots are values at all the deformation conditions: (g) The summary comparison of flow stress; (h) The summary comparison of DRX fraction; (i) The summary comparison of AGS.

The root means square error (RMSE), correlation coefficient (R) and average absolute relative error (AARE) are used to demonstrate the accuracy, the corresponding formulas can be found in literatures [41,43].

Fig. 3. (g)-(i) shows the comparison of the predicted and experimental flow stress, DRX fraction and AGS in all deformation conditions. The RMSE, R, and AARE are given in Table. 3. The model is accurate in content deformation conditions. It can calculate the flow stress and microstructure state during deformation.

Table. 3. The RMSE, R, and AARE of different predicted values.

	RMSE	**R**	**AARE**
Flow Stress	4.2765	0.9894	3.0095%
DRX Fraction	0.0536	0.9512	6.0716%
Average Grain Size	3.1446	0.9401	3.0965%

3.3 Hot processing maps under constant deformation conditions

The η and ξ are solved for different deformation conditions at 0.1, 0.2, ..., and 0.9 strains. The theory can be found in literature [46]. Fig. 4. shows the corresponding hot processing maps. The hot processing maps are superimposed on the η and ξ. The semi-transparent blue region wrapped by the solid line has a negative ξ. The coloured region split by the black dashed line reflects the η. The value on the dashed line represents the η at that location. The hot processing maps can be divided into three characteristic regions. In the low temperature and high strain rate region, the η is low and in instability state. This is related to the suppression of softening mechanism [30]. In the low temperature and low strain rate region or the high temperature and high strain rate region, the η increases as the deformation progresses. The enhanced DRX behavior is activated by deformation [55]. In the high temperature and low strain rate region, the η is high but gradually decreases with deformation. This is attributed to the rapid ending of the DRX and subsequent GG process [56]. The reason for the evolution will be explained later through microstructure characterization.

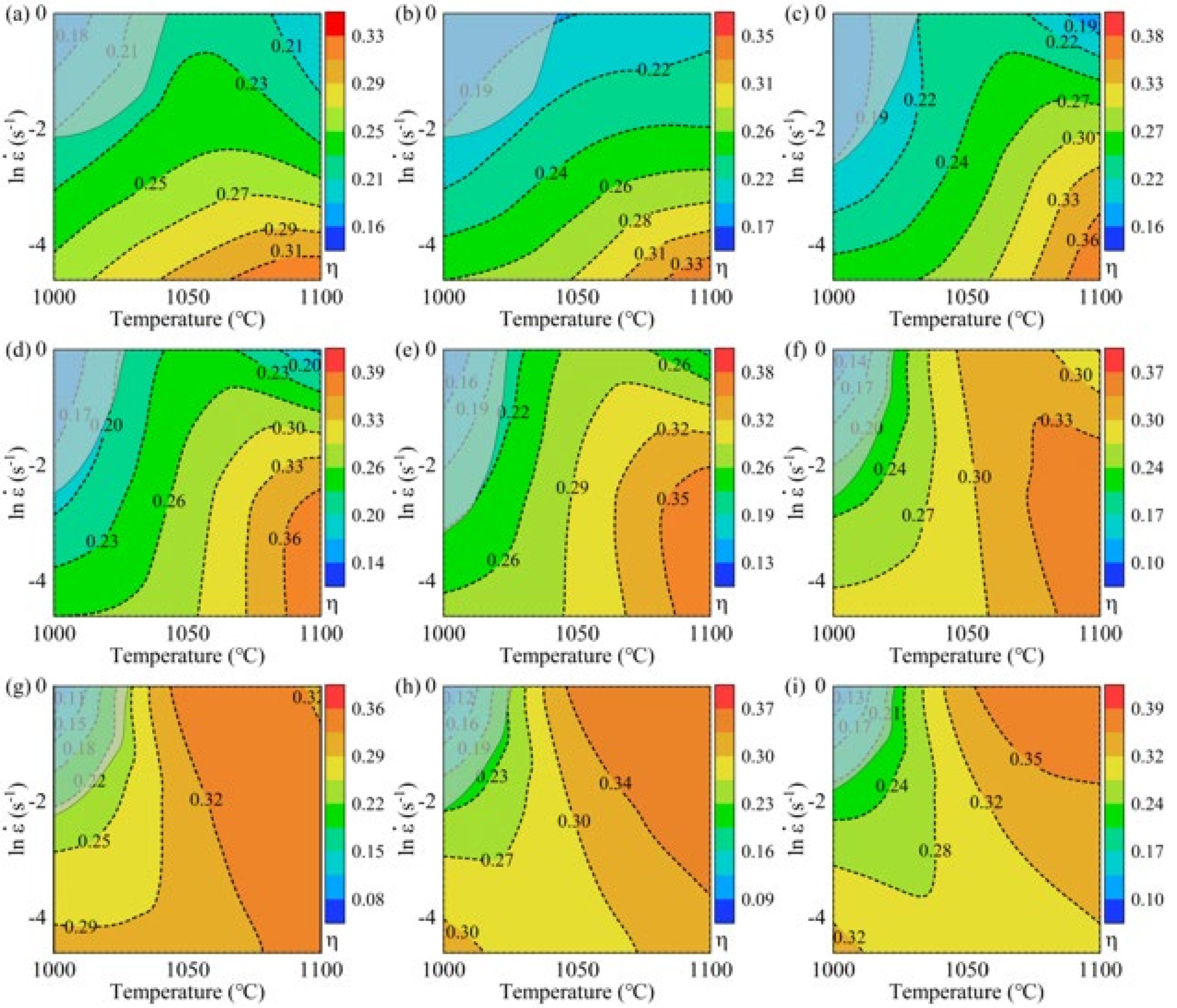

Fig. 4. The hot processing maps (superposition of the η and ξ) at different true strain, where the colored areas represent the η and the semi-transparent blue region represent the ξ<0: (a) At 0.1 true strain; (b) At 0.2 true strain; (c) At 0.3 true strain; (d) At 0.4 true strain; (e) At 0.5 true strain; (f) At 0.6 true strain; (g) At 0.7 true strain; (h) At 0.8 true strain; (i) At 0.9 true strain.

4. The Validation and Application of the Model

This section first validates the prediction accuracy of the hot workability prediction model constructed in section 3. The predicted and experimental values of hot workability under constant deformation conditions are used for comparison. Further, the variation rules of hot workability with deformation conditions and microstructure state are analyzed, combined with the prediction model and experimental data. Finally, the effect of dynamic variation in deformation conditions on the hot workability is determined.

4.1 The hot workability under constant deformation conditions

The η and ξ at 0.1-0.9 true strain are used to train the model. The η and ξ at 0.15-0.85 true strain are used to validate. In addition, the strain, strain rate, and deformation temperature are used as input values (uncoupled microstructure) to train the neural network under the same process and compare the prediction accuracy of the two methods. Fig. 5. (a) and (c) compare the prediction accuracy of the two models for the η. Table. 4. shows the corresponding RMSE, R, and AARE. Fig. 5. (b) and (d) compare the prediction accuracy of the two models for the ξ. Table. 5. shows the corresponding RMSE, R, and AARE. The model coupled with microstructure shows more accurate prediction ability.

Table. 4. The comparison of the prediction ability of η.

	RMSE	**R**	**AARE**
Coupled with microstructure (Train sets)	0.0109	0.9785	3.8144%
Uncoupled with microstructure (Train sets)	0.0206	0.9237	7.4896%
Coupled with microstructure (Test sets)	0.0084	0.98569	3.1165%
Uncoupled with microstructure (Test sets)	0.0186	0.93697	6.6866%

Table. 5. The comparison of the prediction ability of ξ.

	RMSE	**R**	**AARE**
Coupled with microstructure (Train sets)	0.0289	0.96681	2.9209%
Uncoupled with microstructure (Train sets)	0.0756	0.77604	5.8805%
Coupled with microstructure (Test sets)	0.0251	0.97474	3.3848%
Uncoupled with microstructure (Test sets)	0.0625	0.84405	7.3496%

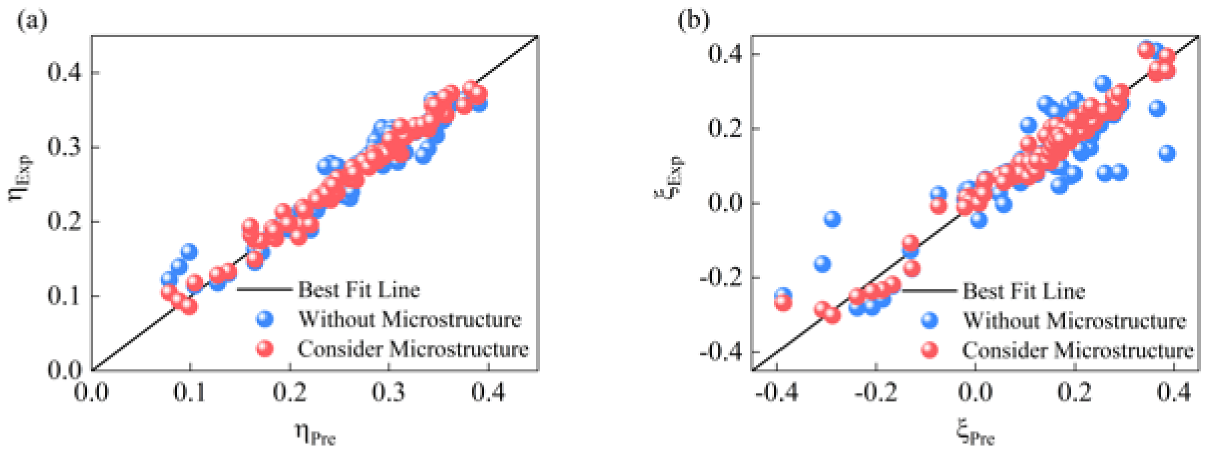

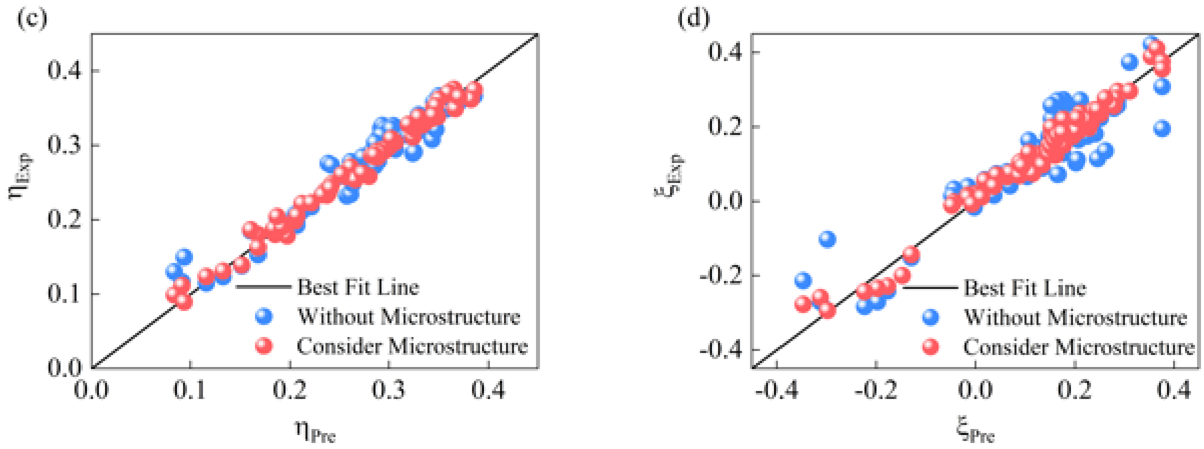

Fig. 5. The prediction accuracy comparison between models coupled with microstructure state and uncoupled with microstructure state: (a) The comparison of the train sets for η; (b) The comparison of the train sets for ξ; (c) The comparison of the test sets for η; (d) The comparison of the test sets for ξ.

In order to further illustrate the relationship between hot workability and microstructure, three deformation conditions (1000°C, 1s^{-1}; 1000°C, 0.01s^{-1}; and 1100°C, 0.01s^{-1}) are selected to characterize. The correlation between the microstructure information and hot workability is investigated.

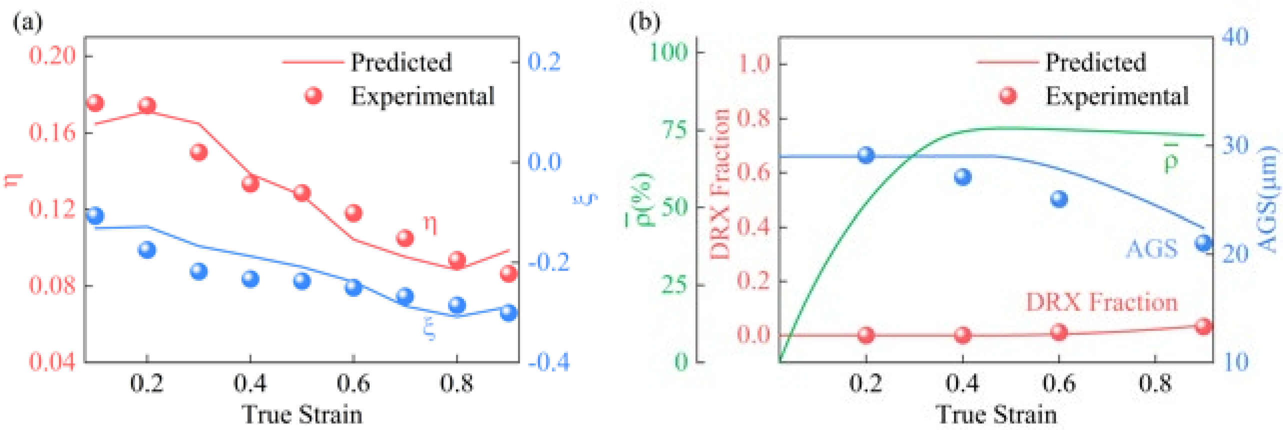

Fig. 6. The comparison of the predicted and experimental values at 1000°C and 1s^{-1}, where the solid lines are the predicted values and the solid dots are the experimental values: (a) the η and ξ evolution, where the red line and dots represent the η and the blue line and dots represent the ξ; (b) the $\bar{\rho}$, DRX fraction, and AGS evolution, where the red line and dots represent the DRX fraction, the blue line and dots represent the AGS and the green line represents the $\bar{\rho}$.

Fig. 6. (a) shows the evolution of the η and ξ at 1000°C and 1s^{-1}. The solid lines are the predicted values, and the dots are the experimental values. The η under the current deformation conditions is low (less than 0.2), and the ξ is less than zero, which means that the deformation instability deteriorates the hot workability. Moreover, the η decreases with deformation. Fig. 6. (b) shows the evolution of the normalized dislocation density, DRX fraction, and

AGS. Only a tiny DRX fraction occurs under the current deformation conditions, leading to a rapid increase and saturation of dislocation density. The softening process cannot effectively dissipate the energy generated within the plastic deformation system.

Fig. 7. (a)-(d) shows the superposition of band contrast and grain boundary maps for 0.2, 0.4, 0.6, and 0.9 true strain at 1000°C and 1s^{-1}. The green solid lines denote the little-angle grain boundaries (LAGBs: 1-2°misorientation angle), the blue solid lines are the medium-angle grain boundaries (MAGBs: 5°-15°misorientation angle), the black solid lines are the high-angle grain boundaries (HAGBs: >15°misorientation angle). The red lines are the Σ3 TBs (statistically obtained according to Brandon's criterion). As deformation proceeds, band substructures characterized by alternating LAGBs and MAGBs along the shear direction gradually develop within the grain (pointed out by the white arrows). The low-temperature and high strain rate inhibit the formation of low-energy structures by self-interaction of dislocations under DRV [57]. It is noteworthy that the band substructures preferentially form near the Σ3 TBs. Under the interaction between the dislocations and TBs, the original Σ3 TBs gradually deviate from the original special orientation relationship (circled by the yellow dashed lines). The macro-shear deformation zone is formed at 0.9 true strain (outlined by the white dashed lines). It is characterized by the clustered of refined DRX grains and substructures, implying deformation instability. The deformation energy is converted into the thermal energy in local regions. The adiabatic heating effect causes inhomogeneous plastic flow in the macroscopic shear deformation zones [58]. In addition, even though a dense cross-arranged dislocation structure is formed, almost no HAGBs are formed. Only a few DRX grains are arranged as a necklace structure along grain boundaries. The bowing out of the original grain boundaries to one side is another piece of evidence (circled by the white dashed lines) [59]. The inhibition of the CDRX may be attributed to the low temperature and high strain rate, which weaken the DRV effect. The substructures accumulated along the slip direction are difficult to further absorb dislocations and form HAGBs by increasing the local misorientation. The original grain boundaries bow outward, driven by the dislocation density difference on both sides. When deformed to a certain degree, the DRX grains form with the assistance of the adiabatic heating effect. In order to illustrate the substructure features, the misorientation information is further statistics along the L1-L2 lines (perpendicular to the direction of the band structure) and the L3-L4 lines (parallel to the direction of the band structure). Fig. 8. (a)-(d) show the local (point to point) and cumulative (point to origin) misorientation angle along the L1-L4 lines shown in Fig. 7. The red line is the cumulative misorientation (statistical from point to origin), and the blue line is the local misorientation (statistical from point to point). For the misorientation information of the L1 and L2 lines, the band substructures consist of densely arranged sub-boundaries with a local misorientation between 0.5-5°. The spacing of the boundaries is about 0.5-3 microns. The cumulative misorientation perpendicular to the deformation

bands exhibits a recurring phenomenon of localized elevation and decrease. Even though the cumulative misorientation increases with distance, it can hardly exceed 15°. The band substructures transform into HAGBs with difficulty, so the CDRX can hardly occur. For the misorientation information of the L3 and L4 lines, the local misorientation angle parallel to the banded substructures' direction rarely exceeds 2°. The dislocations move along the fixed slip planes and directions under the limited opening slip system. The cumulative misorientation increases consistently close to 25°, which may be attributed to the need for coordinated motion between multiple grains under intense plastic deformation.

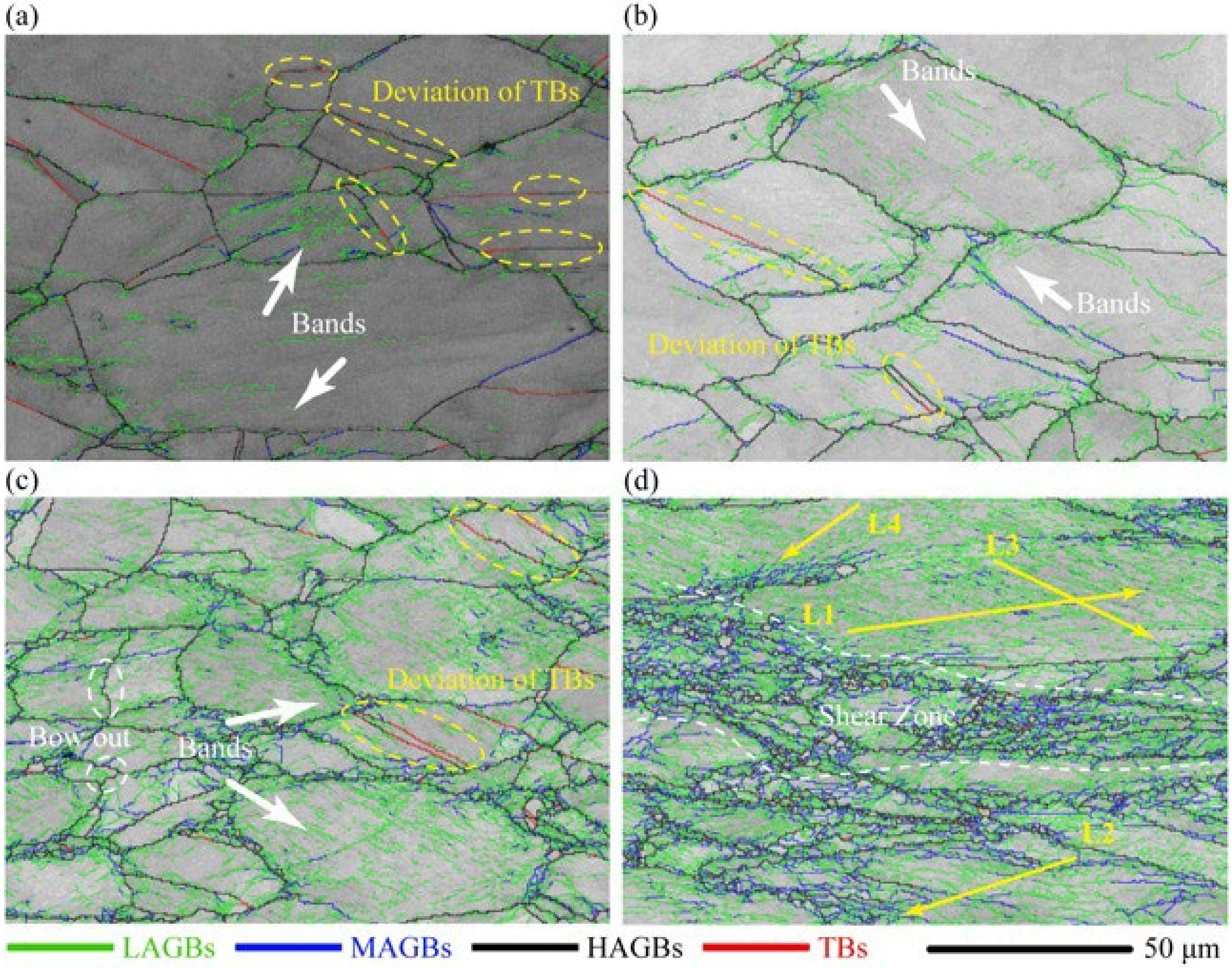

Fig. 7. The superposition of the band contrast and the grain boundary images at 1000°C and $1s^{-1}$ with different deformation degree, where the green lines represent the LAGBs, the blue lines represent the MAGBs, the black lines represent the HAGBs and the red lines represent the TBs: (a) The image at 0.2 true strain; (b) The image at 0.4 true strain; (c) The image at 0.6 true strain; (d) The image at 0.9 true strain.

Fig. 8. (e)-(f) statistic all types of boundaries at 0.2, 0.4, 0.6, and 0.9 true strain. The proportion of the LAGBs and MAGBs increases significantly. The proportion of the HAGBs firstly decreases and finally increases slightly. and the proportion of the Σ3 TBs decreases significantly. The dislocation motion at the beginning of the deformation results

in the formation of sub-grain boundaries. Moreover, with the deformation, the local misorientation gradually increased. The initial annealing TBs inside the grain distorts and loses the original orientation relationship. They are gradually transformed into HAGBs.

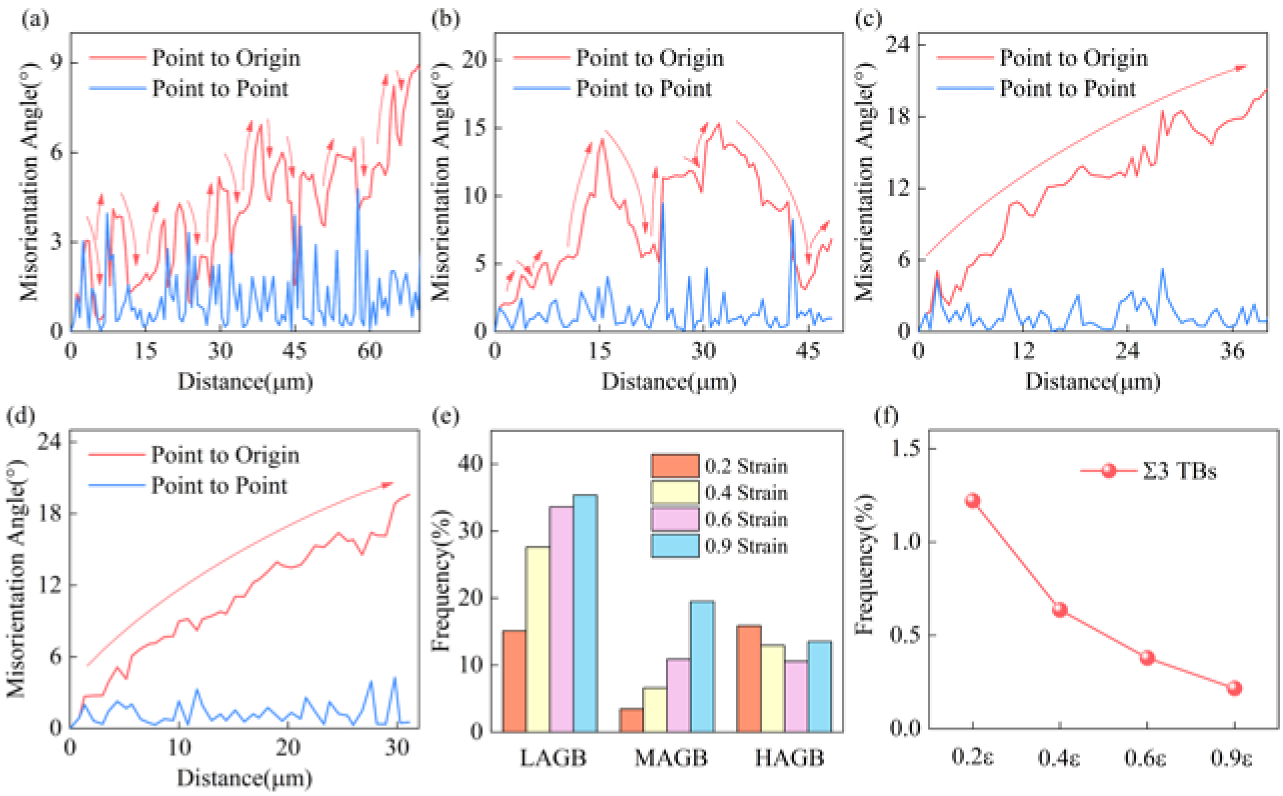

Fig. 8. The statistical information of the local (point to point) and cumulative (point to origin) misorientation angle along the L1-L4 lines shown in Fig. 7 and the frequency of the boundaries with different misorientation angle at 1000°C, 1s^{-1}, and different deformation degree: (a) Along the L1 line; (b)Along the L2 line; (c) Along the L3 line; (d) Along the L4 line; (e) The frequency of the LAGBs, MAGBs, and HAGBs at 0.2, 0.4, 0.6 and 0.9 true strain; (f) The frequency of the Σ3 TBs at 0.2, 0.4, 0.6 and 0.9 true strain.

Fig. 9. (a)-(d) shows the local average misorientation images for 0.2, 0.4, 0.6, and 0.9 true strain at 1000°C, 1s^{-1} deformation conditions. The accumulation of local misorientation denotes the dislocation and storage energy [60]. The storage energy at the beginning of deformation accumulates mainly at grain boundaries, especially at triple grain boundaries (circled by the white dashed lines) for the requirement of coordinated deformation among multiple grains. The deep-colored bands (pointed by the white arrows) have formed across the interior of the grains. This is consistent with the observed microscopic deformation bands. As the deformation proceeds, it gradually extends into the grain interior. The local misorientation continues to increase in most regions. A cell-like low dislocation density structure wrapped by a high local misorientation boundary (pointed out by the yellow arrows) is formed in only a tiny portion. The matching relationship between grain orientation and loading direction leads to preferential slip deformation within

some grains [61]. As the deformation proceeds further, it is gradually homogenized. The area and number of cellular low dislocation density regions decrease. In addition, a few tiny low dislocation density grains are formed along the grain boundaries because of the weak DRX behavior.

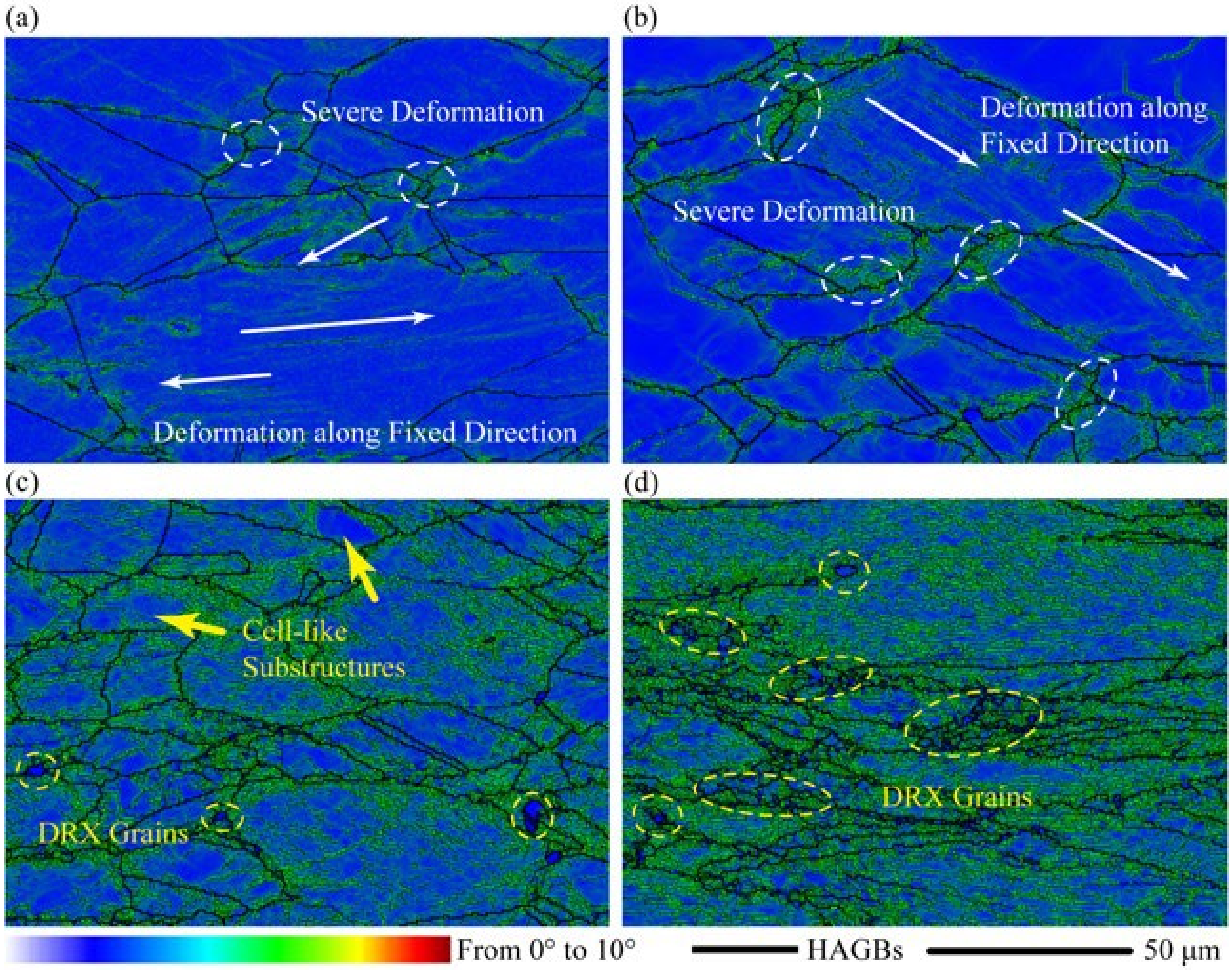

Fig. 9. The local average misorientation images at 1000°C and $1s^{-1}$ with different deformation degree, where the black lines represent the HAGBs and the color from blue to red represent the values of the local average misorientation: (a) The image at 0.2 true strain; (b) The image at 0.4 true strain; (c) The image at 0.6 true strain; (d) The image at 0.9 true strain.

Fig. 10. (a)-(b) show the Schmidt factor images of the {1 1 0} <1 1 1> slip system concerning the loading direction at 0.2 and 0.4 true strain under 1000°C and $1s^{-1}$. The Schmidt factor reflects the relationship between crystal orientation and loading direction for a given slip system [62]. The Schmidt factor reflects the difficulty of grain deformation. A high Schmidt factor represents that the current crystal orientation favors the preferential opening of dislocations along the slip system. After deformation at a $1s^{-1}$ strain rate, the grains with a high Schmidt factor preferentially form a band structure (pointed out by the white arrows) inside the grains. In contrast, only a few LAGBs and MAGBs develop

within the grains with low Schmidt factors (circled by the white dashed lines). As a result, microbands preferentially form in grains whose orientation favors deformation. The preferential opening of fixed slip systems leads to the development of band substructures. In contrast, grains with low Schmidt factors only play a role in coordinating deformation with surrounding grains during initial deformation. As the deformation proceeds, it is gradually homogenized. Eventually, microbands form inside nearly all grains.

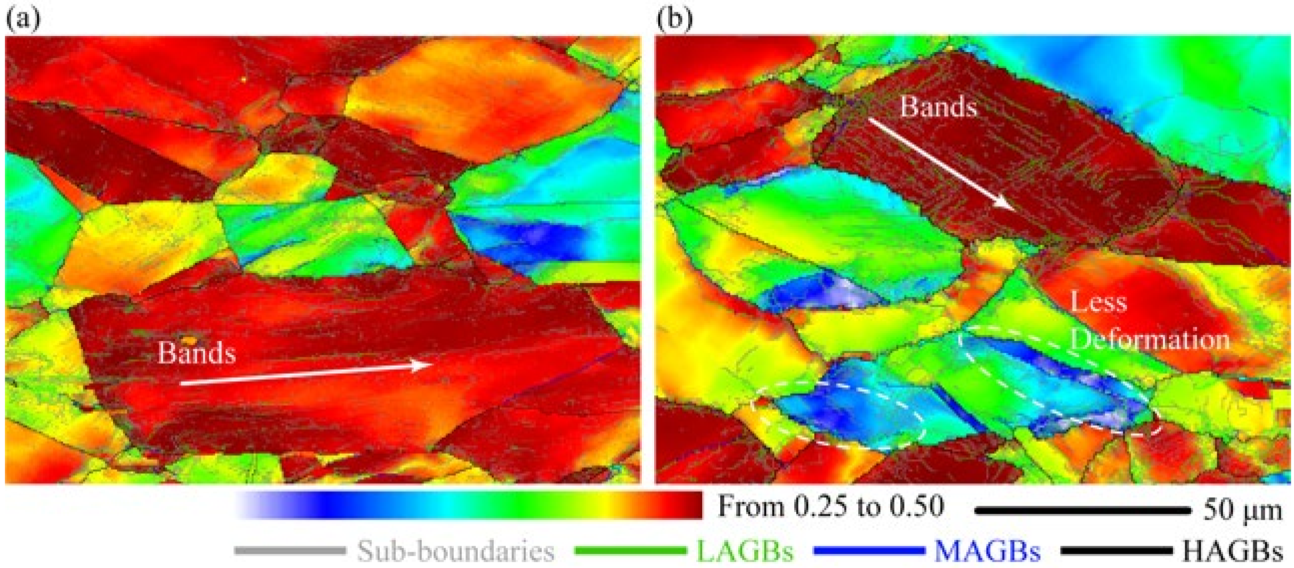

Fig. 10. The Schmidt factor images of the {1 1 0} <1 1 1> slip system concerning the loading direction, where the black lines represent the HAGBs, the gray lines represent the sub-boundaries (0.5°-2°misorientation angle) and the color from blue to red represent the values of Schmidt factor: (a) The image at 0.2 true strain under 1000°C and $1s^{-1}$; (b) The image at 0.4 true strain under 1000°C and $1s^{-1}$.

Overall, the DRV and DRX softening behavior is suppressed at low temperatures and high strain rates, which is manifested by the accumulated dislocation density and a small amount of DRX fraction. Many macro-micro deformation bands are formed, limiting the ability to continue deforming. This results in poor hot workability.

Fig. 11. (a) shows the evolution of the η and ξ at 1000°C and $0.01s^{-1}$. The solid lines are the predicted values, and the dots are the experimental values. The η is 0.25-0.35, increasing with deformation. This means that the DRV and DRX occur in concert. Moreover, the ξ is more significant than zero. This means that the deformation proceeds stably. The energy generated by the deformation is effectively dissipated through microstructure evolution. Fig. 11. (b) shows the evolution of the normalized dislocation density, DRX fraction, and AGS. Under the current deformation conditions, the DRX (close to 60%) occurs. The dislocation density is effectively consumed. In addition, the grain size is significantly refined. The occurrence of DRX effectively improves the hot workability.

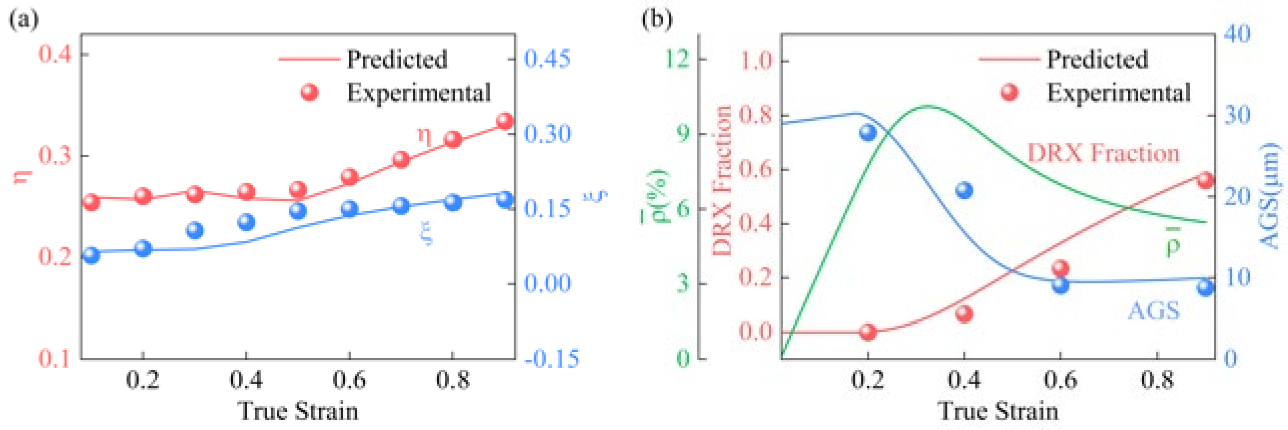

Fig. 11. The comparison of the predicted and experimental values at 1000°C and $0.01s^{-1}$, where solid lines are predicted values and solid dots are experimental values: (a) the η and ξ evolution, where the red line and dots represent the η and the blue line and dots represent the ξ; (b) the $\bar{\rho}$, DRX fraction, and AGS evolution, where the red line and dots represent the DRX fraction, the blue line and dots represent the AGS and the green line represents the $\bar{\rho}$.

Fig. 12. (a)-(d) shows the superposition of the band contrast and the grain boundary images for 0.2, 0.4, 0.6, and 0.9 true strain at 1000°C and $0.01s^{-1}$. The microstructure features significantly differed from those of the $1s^{-1}$. Very few banded substructures are produced. Discontinuous LAGBs and MAGBs form at the deformation's beginning along the original grain boundaries and Σ3 TBs, which leads to the gradual deviation of the Σ3 TBs from the original special orientation relationship (circled by the yellow dashed lines). Some grain boundaries bow outward, driven by the dislocation density gradient on both sides. They are closed by the LAGBs and MAGBs formed near the grain boundaries (circled by the white dashed lines). This indicates the nucleation of DDRX grains under a strain-induced grain boundary migration mechanism. As the deformation proceeds, the substructure network of the LAGBs and MAGBs develops further. The LAGBs and MAGBs are randomly arranged, without exhibiting directional features, and self-confine into tiny cell-like structures similar to the grain morphology (pointed out by pink arrows). A continuous transition from LAGBs to MAGBs and HAGBs shows CDRX characteristics. When deformed to 0.9 true strain, the microstructure consists of DRX and deformed grains. The DRX grains contain two different types. The first type contains the Σ3 TBs (boxed by the white dashed lines), which implies that the formation of DRX grains is accompanied by the long-range migration of grain boundaries, a typical feature of DDRX [63]. Another type does not contain the Σ3 TBs, and are clustered inside the deformed grains (pointed out by the pink lines). Such DRX grains may have developed from substructural networks of the LAGBs and MAGBs [64]. The sub-grains continuously absorb dislocations during deformation and increase the misorientation angle by self-rotation, resulting in DRX grains. This is a typical feature of CDRX. Fig. 13. (a)-(d) show the local (point to point) and cumulative (point to origin)

misorientation angle along the L1-L4 lines shown in Fig. 12. The red line is the cumulative misorientation (statistical from point to origin), and the blue line is the local misorientation (statistical from point to point). Fig. 13. (a)-(b) show the misorientation information of the L1 and L2 lines at 0.6 true strain. The cumulative misorientation changes show prominent step-like characteristics. The LAGBs and MAGBs separate the deformed grains. In addition, many locations have more than 5° local misorientation. Many LAGBs and MAGBs interact to form a substructure network containing multiple sub-grains. Fig. 13. (c)-(d) show the misorientation information of the L3 and L4 lines at 0.9 true strain. The cumulative and local misorientation show similar characteristics as at 0.6 strain. The local misorientation further increases. Many positions with local misorientation exceeding 10° or even 15° occur. As the deformation proceeds, the LAGBs and MAGBs further develop to form HAGBs. Therefore, the DDRX and CDRX act in concert to reduce the internal dislocation density. The high fraction of DRX is consistent with the prediction.

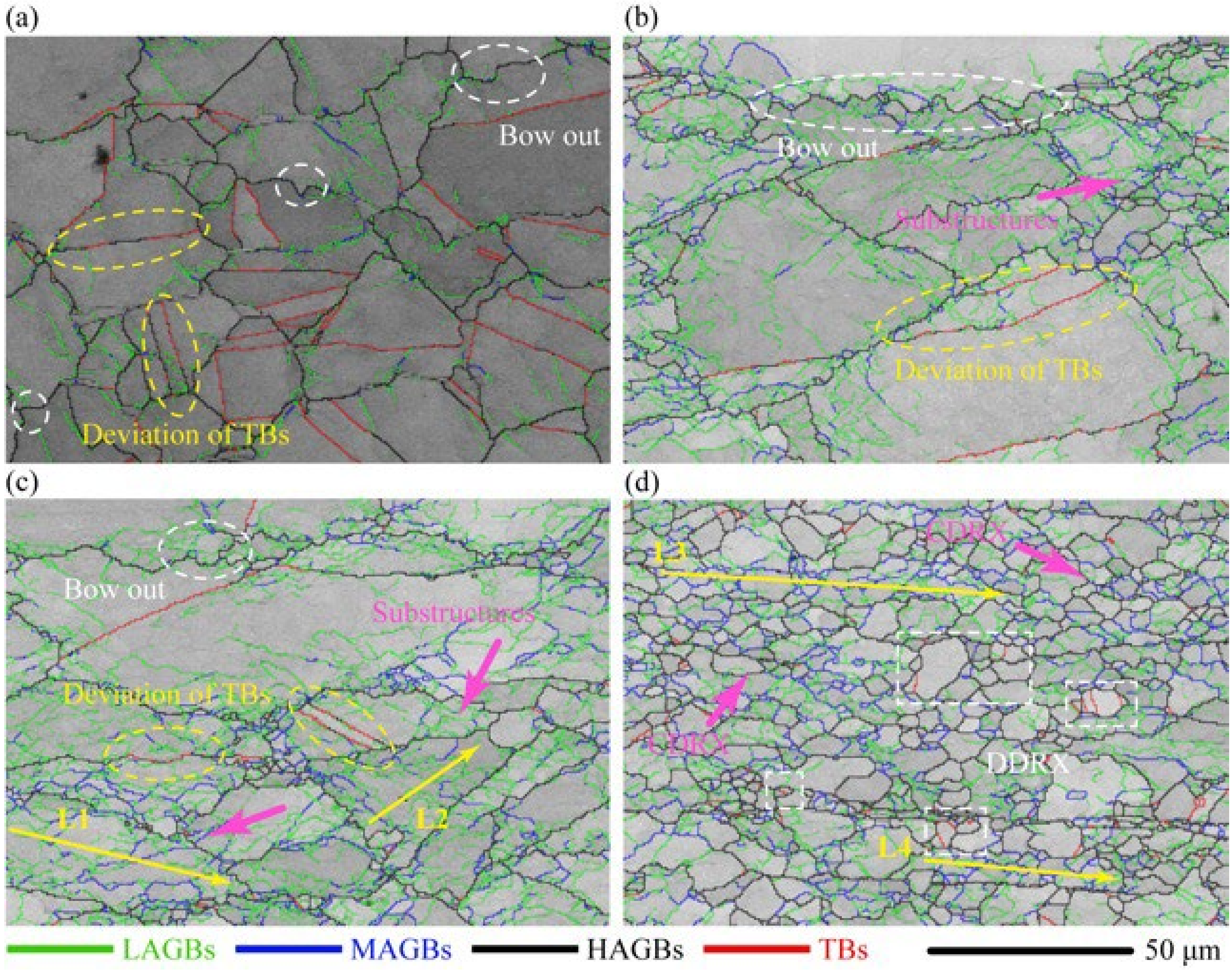

Fig. 12. The superposition of the band contrast and the grain boundary images at 1000°C and 0.01s^{-1} with different deformation degree, where the green lines represent the LAGBs, the blue lines represent the MAGBs, the black lines represent the HAGBs and the red lines represent the TBs: (a) The image at 0.2 true strain; (b) The image at 0.4 true

strain; (c) The image at 0.6 true strain; (d) The image at 0.9 true strain.

Fig. 13. (e)-(f) statistic all types of boundaries at 0.2, 0.4, 0.6, and 0.9 true strain. The proportion of LABGs increases firstly and then decreases finally. The proportion of MAGBs increases gradually with deformation. The proportion of HAGBs decreases firstly and then increases finally. This is attributed to the continuous increase in the misorientation angle of the substructure under the CDRX. The proportion of the Σ3 TBs decreases firstly and then increases slightly when deformed to 0.9 true strain. The decrease is attributed to the distortion of the initial TBs. They lose the original orientation relationship and gradually transform into HAGBs. The subsequent increase is attributed to the migration of the DRX grain boundaries. The Σ3 TBs form within the corresponding grains. The change in boundary characteristics also demonstrates the coupling effect of CDRX and DDRX.

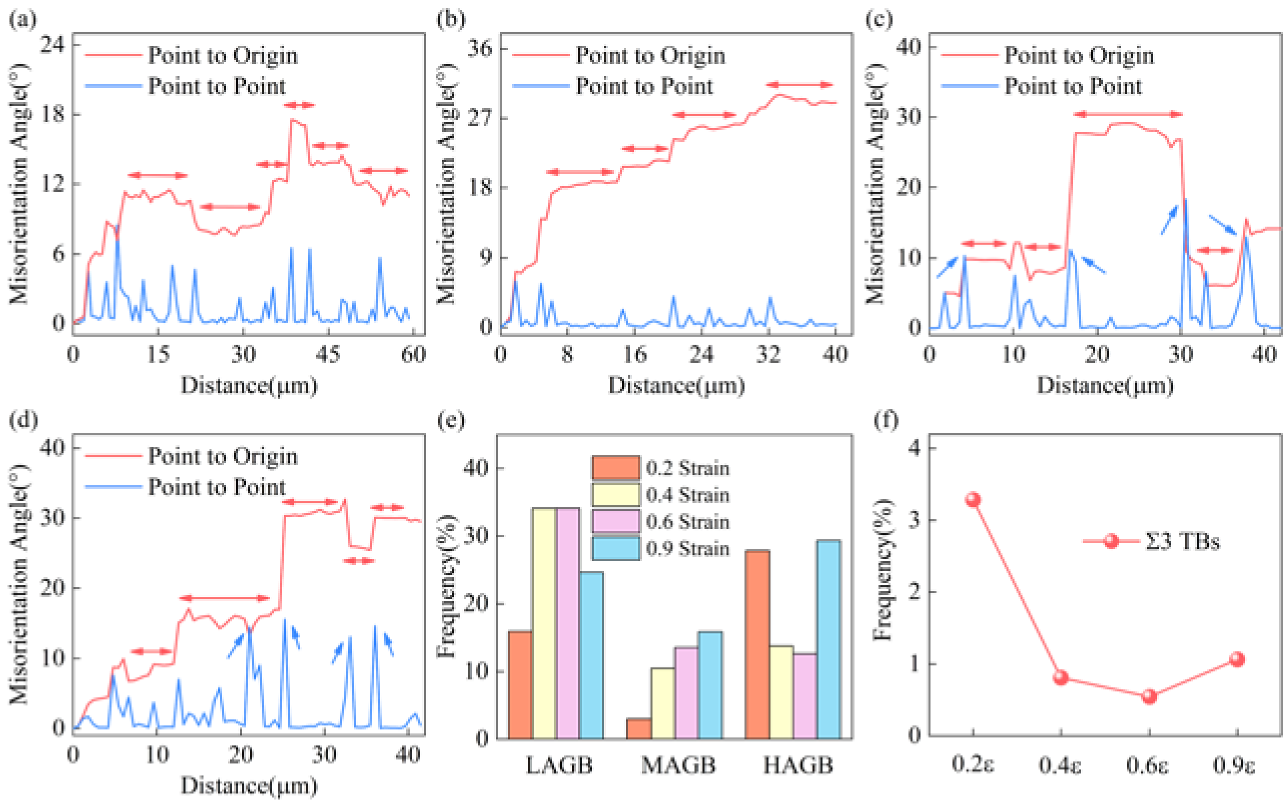

Fig. 13. The statistical information of the local (point to point) and cumulative (point to origin) misorientation angle along the L1-L4 lines shown in Fig. 12 and the frequency of the boundaries with different misorientation angle at 1000°C, 0.01s^{-1}, and different deformation degree: (a) Along the L1 line; (b)Along the L2 line; (c) Along the L3 line; (d) Along the L4 line; (e) The frequency of the LAGBs, MAGBs, and HAGBs at 0.2, 0.4, 0.6 and 0.9 true strain; (f) The frequency of the Σ3 TBs at 0.2, 0.4, 0.6 and 0.9 true strain.

Boundaries' local misorientation angle statistics at 1000°C and 0.01s^{-1}: (a) 0-5°; (b) 5-60°.

Fig. 14. (a)-(d) shows the local average misorientation images for 0.2, 0.4, 0.6, and 0.9 true strain at 1000°C, 0.01s^{-1} deformation conditions. Unlike the 1000 °C, 1s^{-1} deformation condition, many cell-like low dislocation density

structures wrapped by high local misorientation angle boundaries are formed. The dislocations have sufficient time to form substructures by climbing and cross-slip under the DRV. In addition, some of the original grain boundaries bow outward and are closed by the HAGBs. The dislocation density gradient induces the further migration of the grain boundaries [65]. When deformed to the 0.9 true strain, many equiaxed grains appear because of the coupling effect of the CDRX and DDRX.

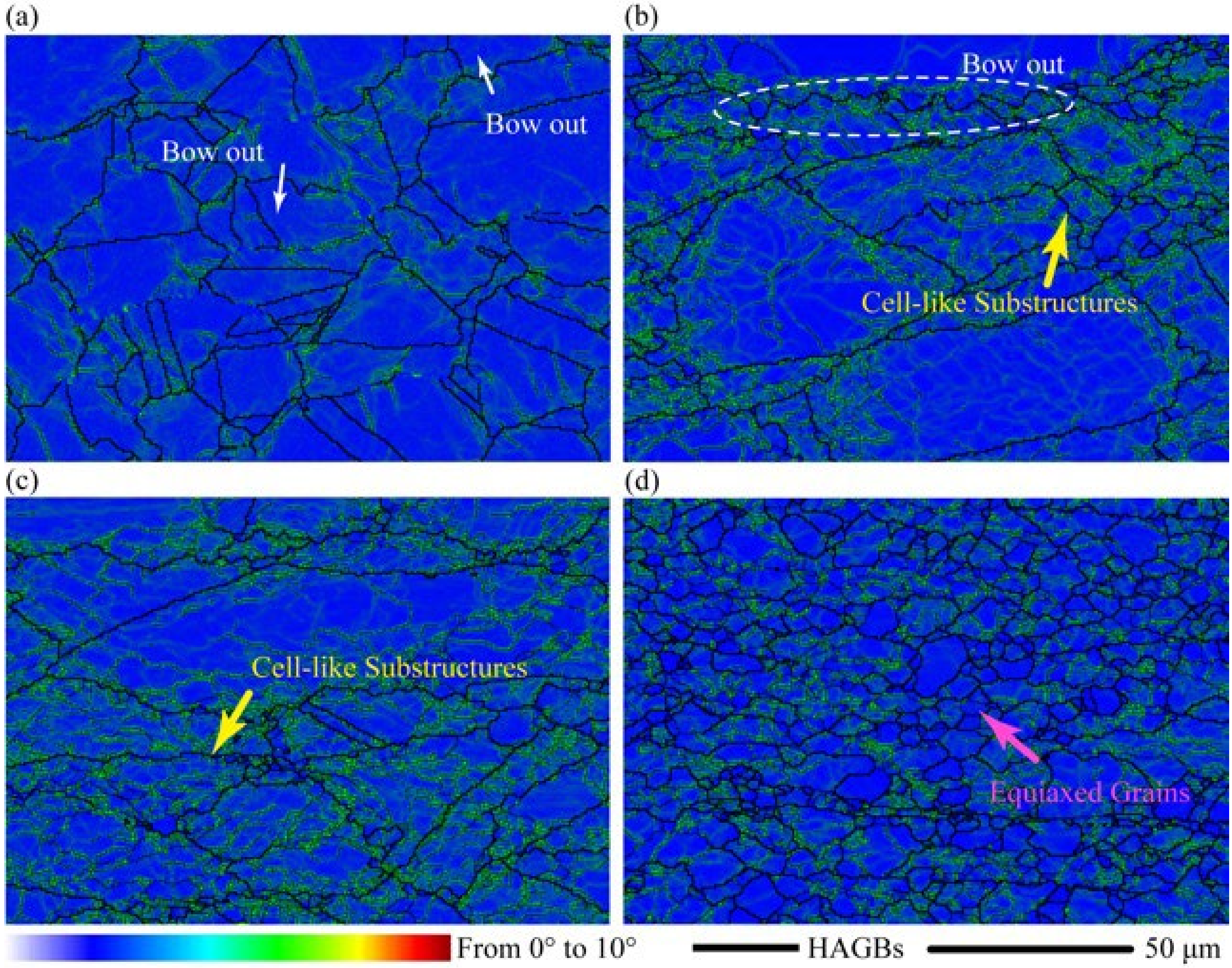

Fig. 14. The local average misorientation images at 1000°C and 0.01s^{-1} with different deformation degree, where the black lines represent the HAGBs and the color from blue to red represent the values of the local average misorientation: (a) The image at 0.2 true strain; (b) The image at 0.4 true strain; (c) The image at 0.6 true strain; (d) The image at 0.9 true strain.

Overall, under these deformation conditions, the DRX ability is not strong. At the beginning of the deformation, the primary softening mechanism is dislocation rearrangement under the DRV. This is manifested as the continuous network substructures within the grain, resulting in the initial low η. However, as the deformation proceeds, DRX continues, consistently reducing the dislocation density, increasing the DRX fraction, and refining the grain size. This is manifested by the gradual replacement of the original deformed grains by many DRX grains. The hot workability gradually improves as the deformation energy is efficiently dissipated.

Fig. 15. (a) shows the evolution of the η and ξ at the 1100°C and 0.01s^{-1}. The overall η is in the range of 0.3-0.4, implying a significant DRX. The ξ is greater than zero. Notably, as the deformation progresses, the η increases to a peak and then decreases gradually. The significant grain growth deteriorates the hot workability after the rapid saturation of the DRX. Fig. 15. (b) shows the evolution of the normalized dislocation density, DRX fraction, and AGS. As the deformation proceeds, the pronounced DRX occurs (close to 80%). The high temperature and low strain rate provided sufficient time and driving force to consume the dislocation density. In addition, the AGS decreases rapidly in the early deformation stage. However, it exhibits a slow increase in the later stages of deformation because of the competitive process between the DRX and GG.

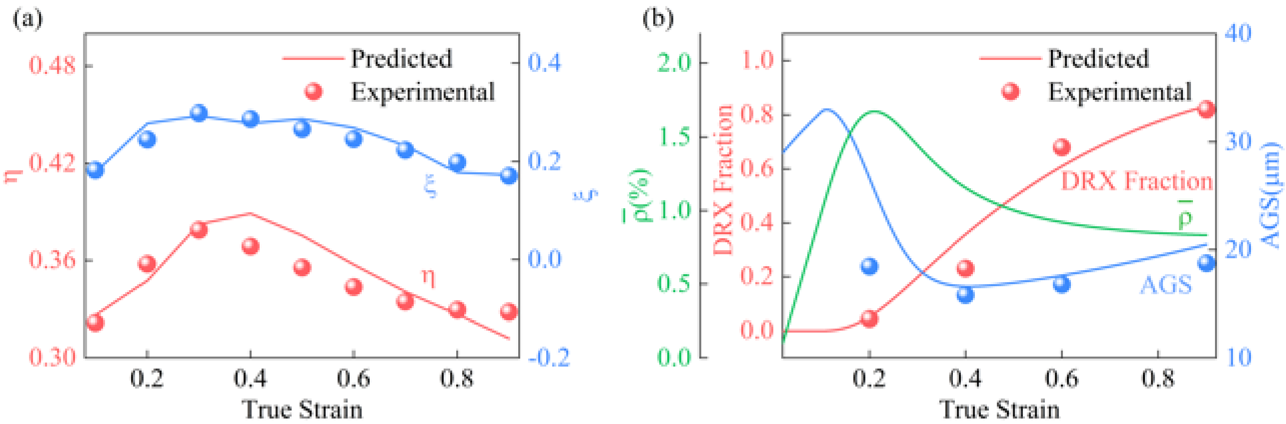

Fig. 15. The comparison of the predicted and experimental values at 1100°C and 0.01s^{-1}, where the solid lines are the predicted values and the solid dots are the experimental values: (a) the η and ξ evolution, where the red line and dots represent the η and the blue line and dots represent the ξ; (b) the $\bar{\rho}$, DRX fraction, and AGS evolution, where the red line and dots represent the DRX fraction, the blue line and dots represent the AGS and the green line represents the $\bar{\rho}$.

Fig. 16. (a)-(d) shows the superposition of the band contrast and grain boundary images for 0.2, 0.4, 0.6, and 0.9 true strain at 1100°C and 0.01s^{-1}. The original grain boundaries bow out significantly. The number and size of bow-out grain boundaries are increased, which are closed through the LAGBs and MAGBs (circled by the white dashed lines). This is consistent with the DDRX nucleation, characterized by the strain-induced grain boundary migration. As the deformation proceeds, more Σ3 TBs are generated. The Σ3 TBs are formed mainly in the low dislocation density grains (pointed out by the blue arrows), accompanied by the grain boundary migration. In addition, at the beginning of deformation, the original Σ3 TBs are the main substructure formation region (circled by the yellow dashed lines). However, as the deformation proceeds, the substructure network is not fully developed. The substructure network

gradually disintegrates (pointed out by the pink arrows). The formation of the $\Sigma 3$ TBs and the bowing-out grain boundary indicates that the DDRX mechanism dominates the current DRX process [65]. Fig. 17. (a)-(d) statistic the local (point to point) and cumulative (point to origin) misorientation angle along the L1-L4 lines shown in Fig. 16. The red line is the cumulative misorientation (statistical from point to origin), and the blue line is the local misorientation (statistical from point to point). Fig. 17. (a) shows the misorientation information of the L1 line at 0.4 true strain. The local misorientation angle partially reaches 2-5° or even more than 5°, which implies forming a certain number of LAGBs and MAGBs. The cumulative misorientation angle exhibits a noticeable step-like feature, suggesting the formation of a cell-like substructure network [66]. However, the step length, which denotes the sub-grain size, is much larger than that of the 1000 °C, 0.01 s^{-1} deformation condition. Fig. 17. (b) shows the misorientation information of the L2 line at 0.6 true strain. The proportion of LAGBs and MAGBs is reduced compared to the 0.4 strain condition. Fig. 17. (c)-(d) show the misorientation information of the L3 and L4 lines at 0.9 true strain. Only a small number of locations have local misorientation angles exceeding 5°. The cumulative misorientation angle also decreases compared with that at 0.4 and 0.6 strain, suggesting that the substructure undergoes self-disintegration through the interactions between dislocations. Notably, none of the cumulative misorientation angles exceed 15°, implying the difficulty of forming HAGBs within the deformed grains. The above phenomenon also indicates that the DDRX dominates the DRX process.

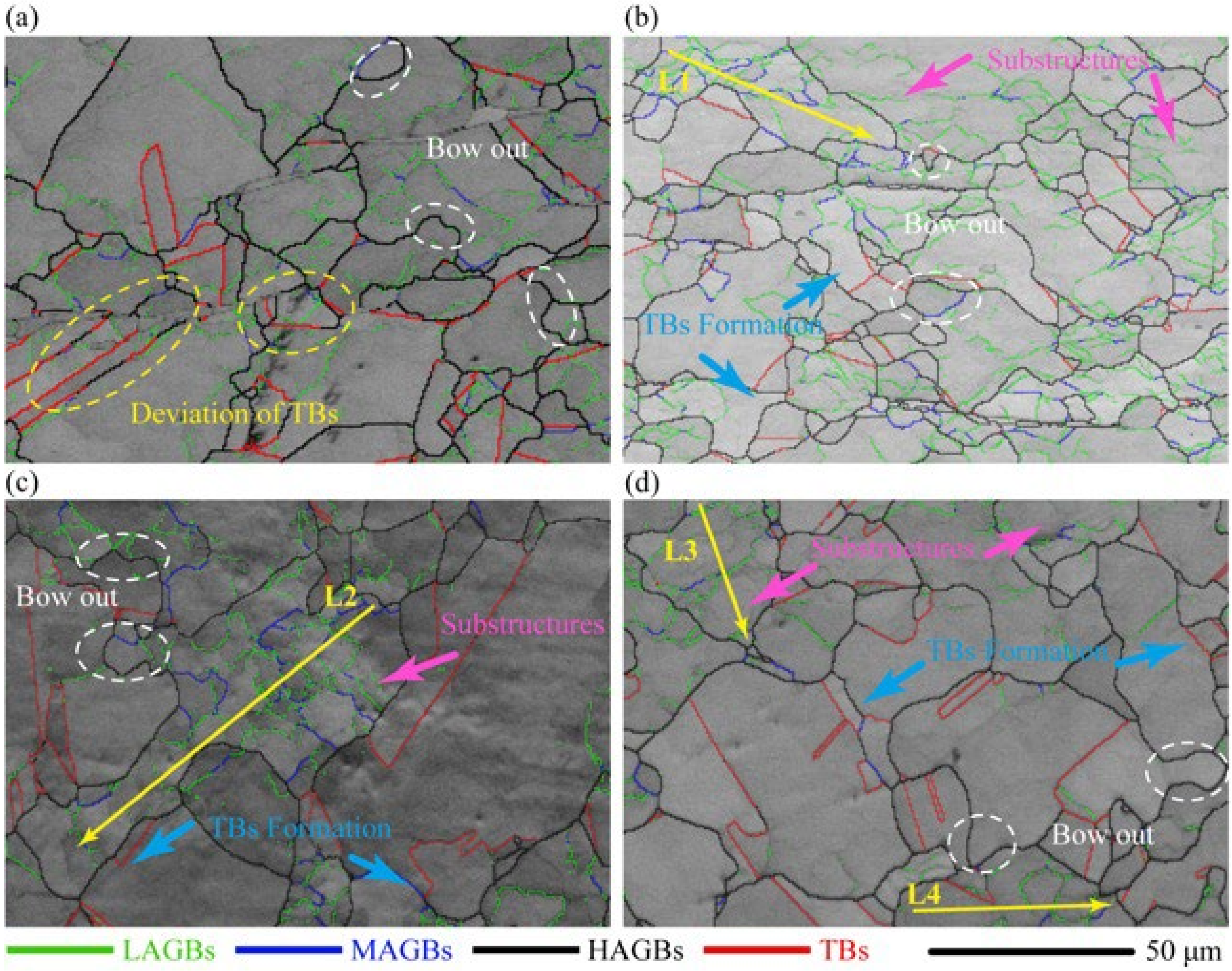

Fig. 16. The superposition of the band contrast and grain boundary images at 1100℃ and 0.01s^{-1} with different deformation degree, where the green lines represent the LAGBs, the blue lines represent the MAGBs, the black lines represent the HAGBs and the red lines represent the TBs: (a) The image at 0.2 true strain; (b) The image at 0.4 true strain; (c) The image at 0.6 true strain; (d) The image at 0.9 true strain.

Fig. 17. (e)-(f) statistic all types of boundaries at 0.2, 0.4, 0.6, and 0.9 true strain. The proportion of the LAGBs and MAGBs decreases, and the proportion of the HAGBs increases with deformation. In particular, the proportion of the Σ3 TBs increases significantly with strain. This again indicates a drastic DDRX phenomenon. First, the substructures within the grain are effectively consumed during the nucleation and growth process of the DDRX grains. In addition, a certain number of Σ3 TBs are generated, accompanied by the long-range migration of the grain boundaries.

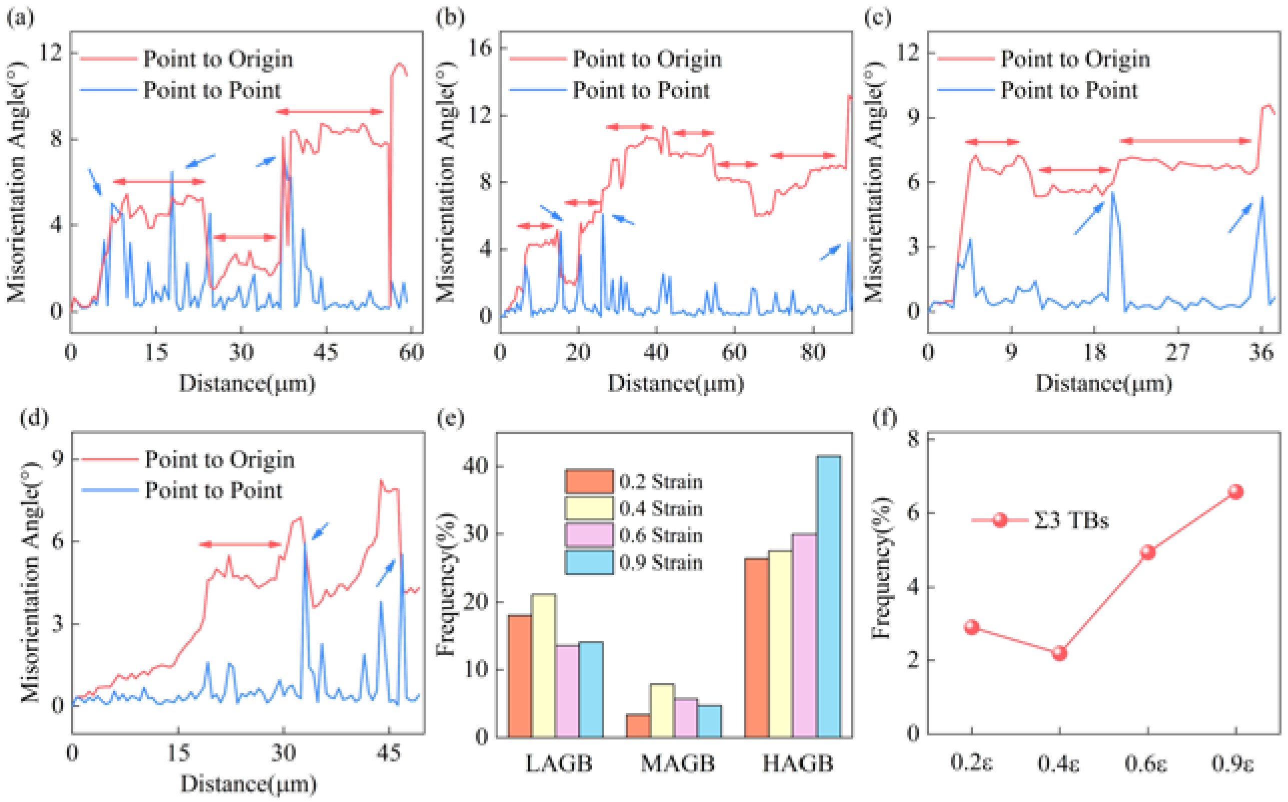

Fig. 17. The statistical information of the local (point to point) and cumulative (point to origin) misorientation angle along L1-L4 lines shown in Fig. 16 and the frequency of the boundaries with different misorientation angle at 1100°C, $0.01s^{-1}$, and different deformation degree: (a) Along the L1 line; (b)Along the L2 line; (c) Along the L3 line; (d) Along the L4 line; (e) The frequency of the LAGBs, MAGBs, and HAGBs at 0.2, 0.4, 0.6 and 0.9 true strain; (f) The frequency of the Σ3 TBs at 0.2, 0.4, 0.6 and 0.9 true strain.

Fig. 18. (a)-(d) shows the local average misorientation images at 0.2, 0.4, 0.6, and 0.9 true strain for 1100°C, $0.01s^{-1}$ deformation conditions. Many blue DRX grains with low dislocation density replace the original deformed grains. The substructure network formed at the early deformation stage gradually decomposes or is subsumed.

Overall, the current deformation conditions of high deformation temperature and low strain rate bring enough thermal activation energy and action time [66, 67]. DDRX continues to occur, resulting in a high overall η. However, at the later stage of deformation, DRX rapidly reaches saturation. The dislocation is consumed by long-range grain boundary migration. The grains grow significantly. This leads to a gradual decrease in the η.

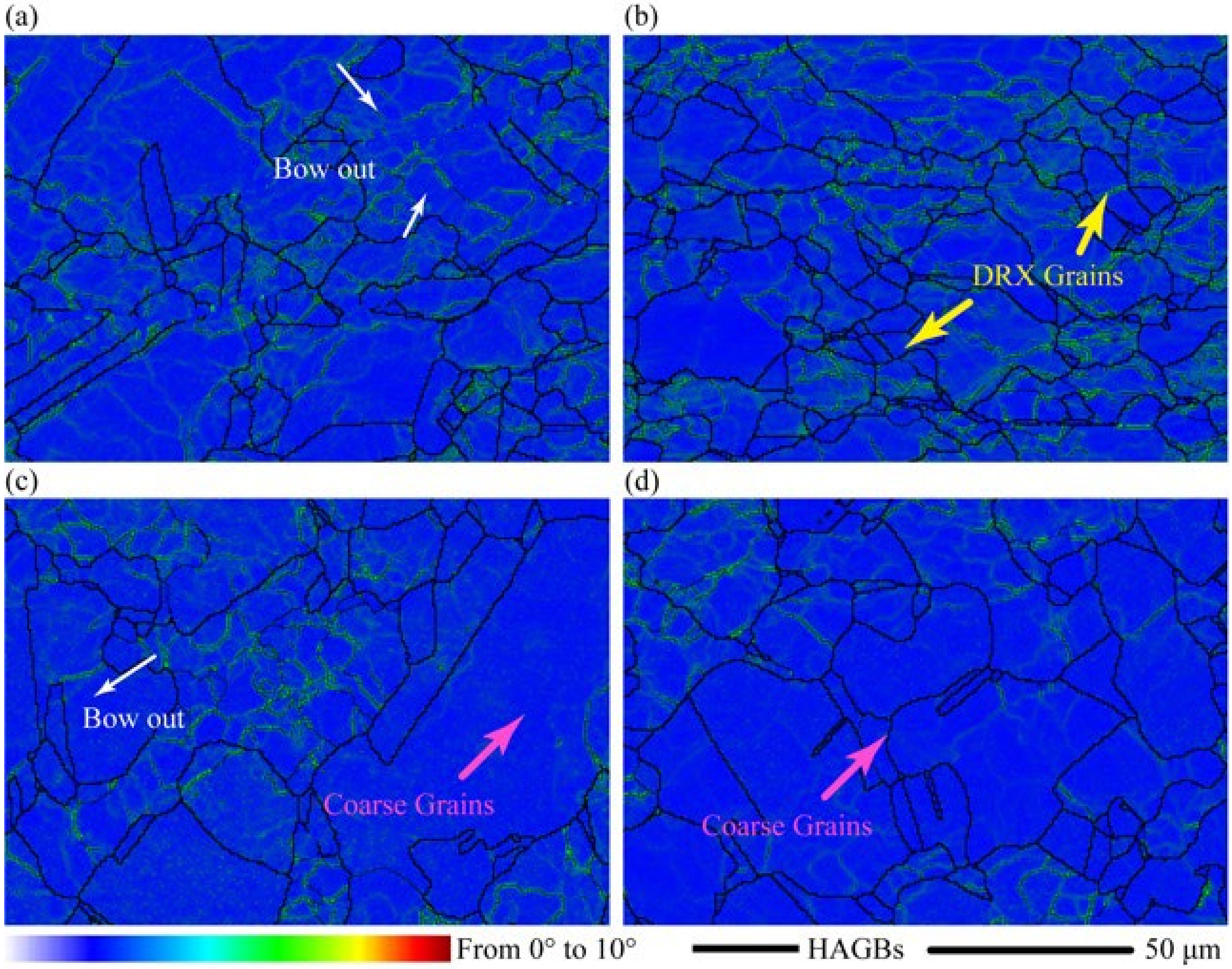

Fig. 18. The local average misorientation images at 1100℃ and 0.01s^{-1} with different deformation degree, where the black lines represent the HAGBs and the color from blue to red represent the values of the local average misorientation: (a) The image at 0.2 true strain; (b) The image at 0.4 true strain; (c) The image at 0.6 true strain; (d) The image at 0.9 true strain.

4.2 The Hot workability prediction under non-constant deformation conditions

4.2.1 Under the strain rate continuous increase deformation conditions

Fig. 19. (a)-(d) shows the flow stress, DRX fraction, normalized dislocation density, and AGS curves under the deformation state of strain rate continuous increase. The black dashed lines show the results under steady-state deformation conditions. The colored solid lines are the predicted results. The dots are the corresponding experimental values. The deformation temperature is 1000 °C. Firstly, the sample is deformed to 0.4 true strain at 0.01 s^{-1}, followed by a increase of the strain rate to 1 s^{-1} during successive deformations. Table. 1. demonstrates the experimental conditions. In the type 1 condition, the strain rate undergoes a transient increase. In the type 2 condition, the strain rate completes the increase at 0.6 true strain. In the type 3 condition, the strain rate completes the increase at 0.9 true strain.

Along with the increase of strain rate, the flow stress firstly rises rapidly and gradually tends to saturation. The elevation of flow stress is attributed to two aspects. One is that the change of deformation conditions directly affects the initial resistance of dislocation slip [68, 69]. The other is that the change induces the corresponding change of microstructure, such as dislocation density and grain size, which affects the short-range obstacle of dislocation motion [70, 71]. The dislocation density shows a similar trend to the flow stress. The DRX curves show that the continuous increase of strain rate suppresses the DRX effect. However, the grain size refinement is not inhibited. Both the DRX fraction and DRX grain size affect the grain refinement [72, 73]. A continuous increase in strain rate reduces the DRX fraction and the DRX grain size. Thus, type 3 exhibits a more pronounced grain refinement than 1000 °C, 0.01 s^{-1}. Fig. 19. (e)-(f) shows the changes of the η and ξ under the above deformation conditions. When the strain rate continuously increases, the η undergoes a corresponding decrease. However, they are all higher than the power dissipation rate for the 1000 °C, 1 s^{-1} deformation condition. This shows that even if the final deformation conditions are the same, changes in the history of the deformation conditions can also affect the hot workability. A certain degree of low strain rate deformation before high strain rate deformation is beneficial for improving the hot workability. The change in the ξ also proves it.

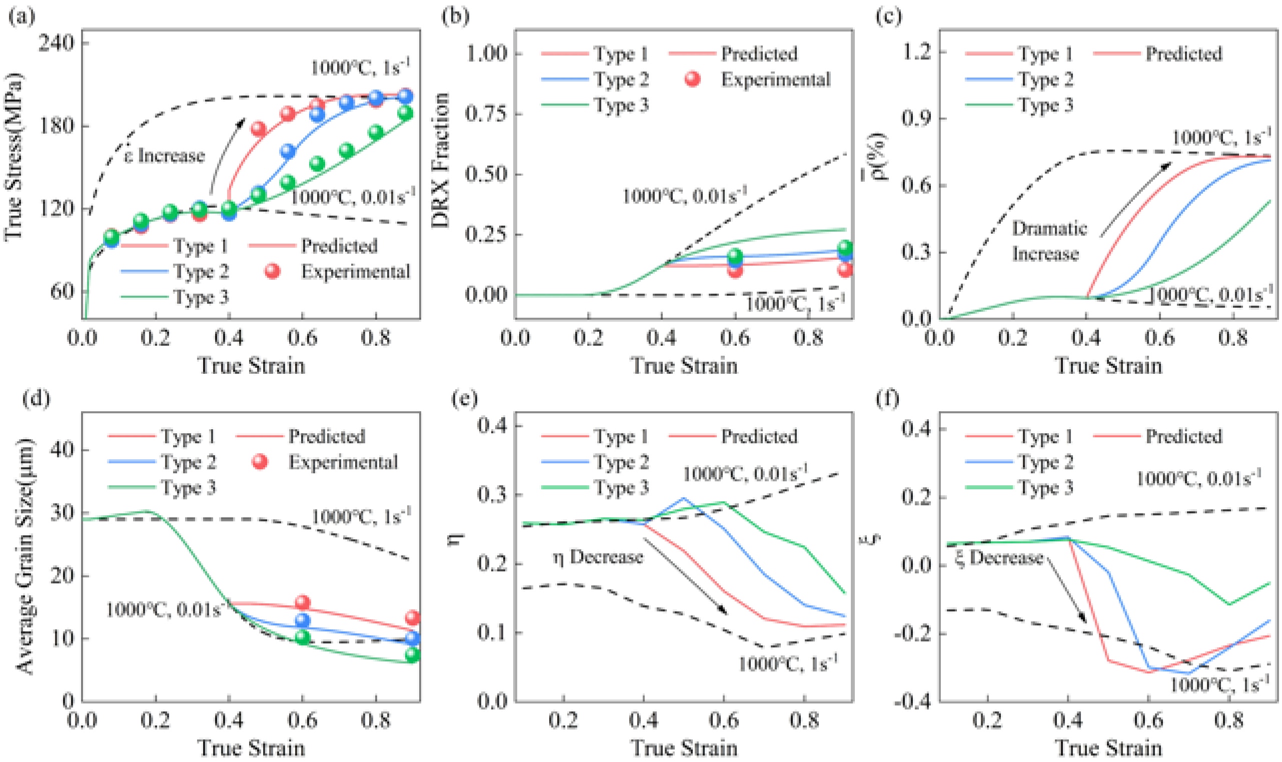

Fig. 19. The predicted flow stress, DRX fraction, normalized dislocation density, AGS, hot workability, and the corresponding experimental data at 1000°C and a continuous increase in strain rate from 0.01s^{-1} to 1s^{-1}, where the solid lines are the predicted values, the solid dots are the experimental values and the colors represent different

conditions of strain rate changing shown in Table. 1: (a) The flow stress evolution; (b) The DRX fraction evolution; (c) The Normalized dislocation density evolution; (d) The AGS evolution; (e) The η evolution; (f) The ξ evolution.

Fig. 20. (a)-(f) shows the superposition of the band contrast and the grain boundary images for 0.6 and 0.9 true strain at the conditions mentioned in Table. 1. (type 1, 2, and 3). Notably, in all cases, no microbands form inside the deformed grains. Instead, many substructure networks consisting of a mixture of the LAGBs and MAGBs (pointed out by the pink arrows) are formed. Moreover, with deformation up to 0.9 true strain, some discontinuous HAGBs are formed inside some grains. Some DRX grains surrounded by the HAGBs even form inside some grains (indicated by the pink dashed circles). This differs entirely from the microstructure formed under the $1s^{-1}$ constant deformation condition. In addition, some DRX grains containing substructures inside are formed at the deformed grains boundaries (circled by the white dashed lines). The above phenomena indicate that the substructure and DRX structure formed during the initial low strain rate deformation process significantly affects their evolution after the strain rate increases. As shown in Fig. 12. (b), a substructure network consisting of LAGBs and MAGBs is formed when deformed to 0.4 true strain at $0.01s^{-1}$. Fig. 21. (a)-(b) show the Schmidt factor maps of the {1 1 0} <1 1 1> slip system concerning the loading direction when deformed to 0.2 and 0.4 true strains at a strain rate of $0.01s^{-1}$. Complex substructures are formed inside grains with high Schmidt factors. After the strain rate increases, the partial slip system preferentially opens. Dislocations increase and start to move in a fixed direction. However, the fixed-direction dislocation motion is impeded by the substructure networks. Other slip systems are activated sequentially to coordinate the polycrystalline deformation. The initial substructure networks absorb the dislocations and further develops. Some HAGBs are formed with the increase of the misorientation angle. In addition, the DDRX grains are formed by strain-induced grain boundary migration at low strain rates. The DRX grains coordinate the deformation of the surrounding grains during the subsequent high strain rate deformation. As a result, some refined grains with internal substructures are formed along the grain boundary locations. Finally, a mixture of substructure-containing and non-substructure-containing refined grains is exhibited. In summary, the initial substructures and DRX grains formed at low strain rates significantly alleviate the deformation concentration phenomenon and improve the hot workability after the strain rate increases. The η and ξ show an increasing trend compared to the constant deformation process at $1s^{-1}$. Fig. 22. (a)-(d) statistic the local (point to point) and cumulative (point to origin) misorientation angle along the L1-L4 lines shown in Fig. 20. The misorientation information is different from that in the $1s^{-1}$ constant deformation condition. Many locations with local misorientation angles exceeding 5° or even 15° appear. This again indicates the formation of abundant MAGBs and HAGBs within the grain.

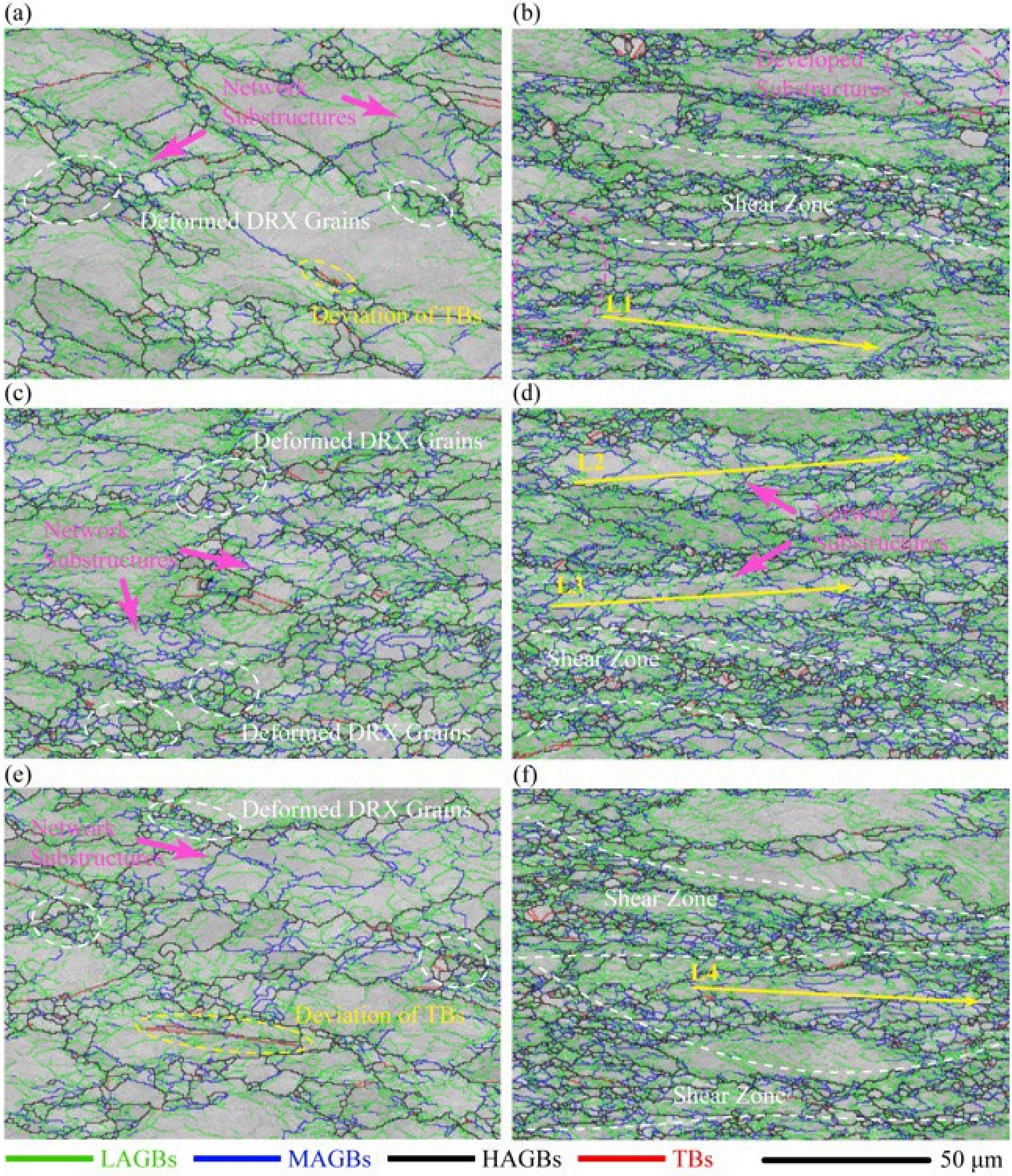

Fig. 20. The superposition of the band contrast and the grain boundary images at 1000℃ and a continuous increase in strain rate from $0.01s^{-1}$ to $1s^{-1}$ with different changing conditions and deformation degree, where the green lines represent the LAGBs, the blue lines represent the MAGBs, the black lines represent the HAGBs and the red lines represent the TBs: (a) The image for the type 1 changing condition at 0.6 true strain; (b) The image for the type 1 changing condition at 0.9 true strain; (c) The image for the type 2 changing condition at 0.6 true strain; (d) The

image for the type 2 changing condition at 0.9 true strain; (e) The image for the type 3 changing condition at 0.6 true strain; (f) The image for the type 3 changing condition at 0.9 true strain.

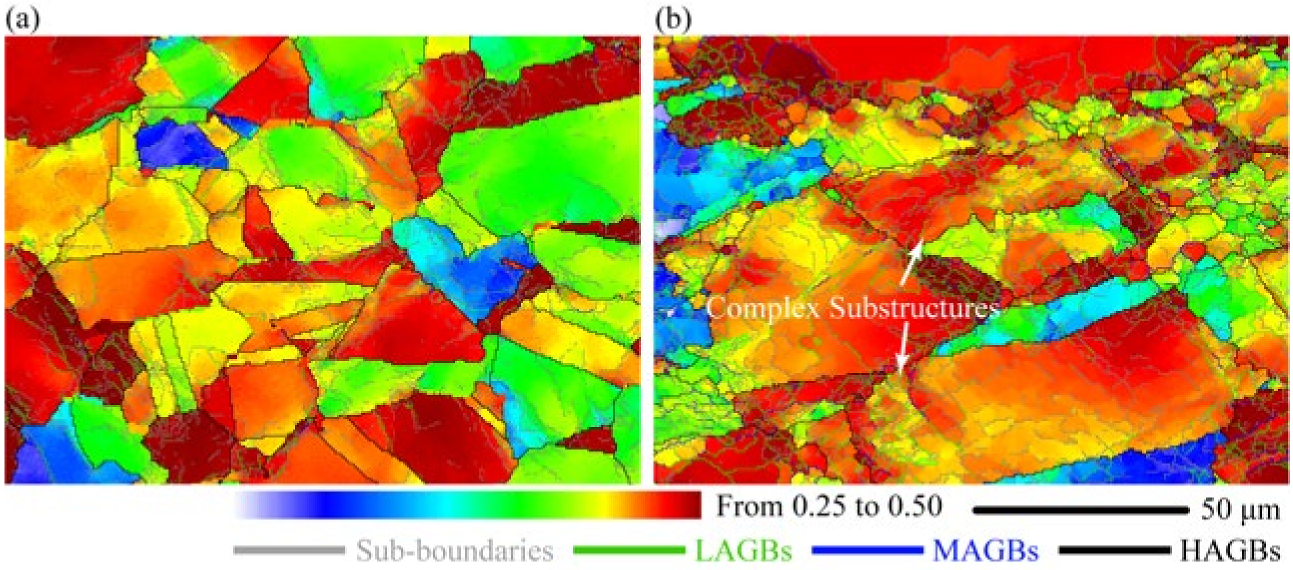

Fig. 21. The Schmidt factor images of the {1 1 0} <1 1 1> slip system concerning the loading direction, where the black lines represent the HAGBs, the gray lines represent the sub-boundaries (0.5°-2°misorientation angle) and the color from blue to red represent the values of Schmidt factor: (a) The image at 0.2 true strain under 1000℃ and $0.01s^{-1}$; (b) The image at 0.4 true strain under 1000℃ and $0.01s^{-1}$.

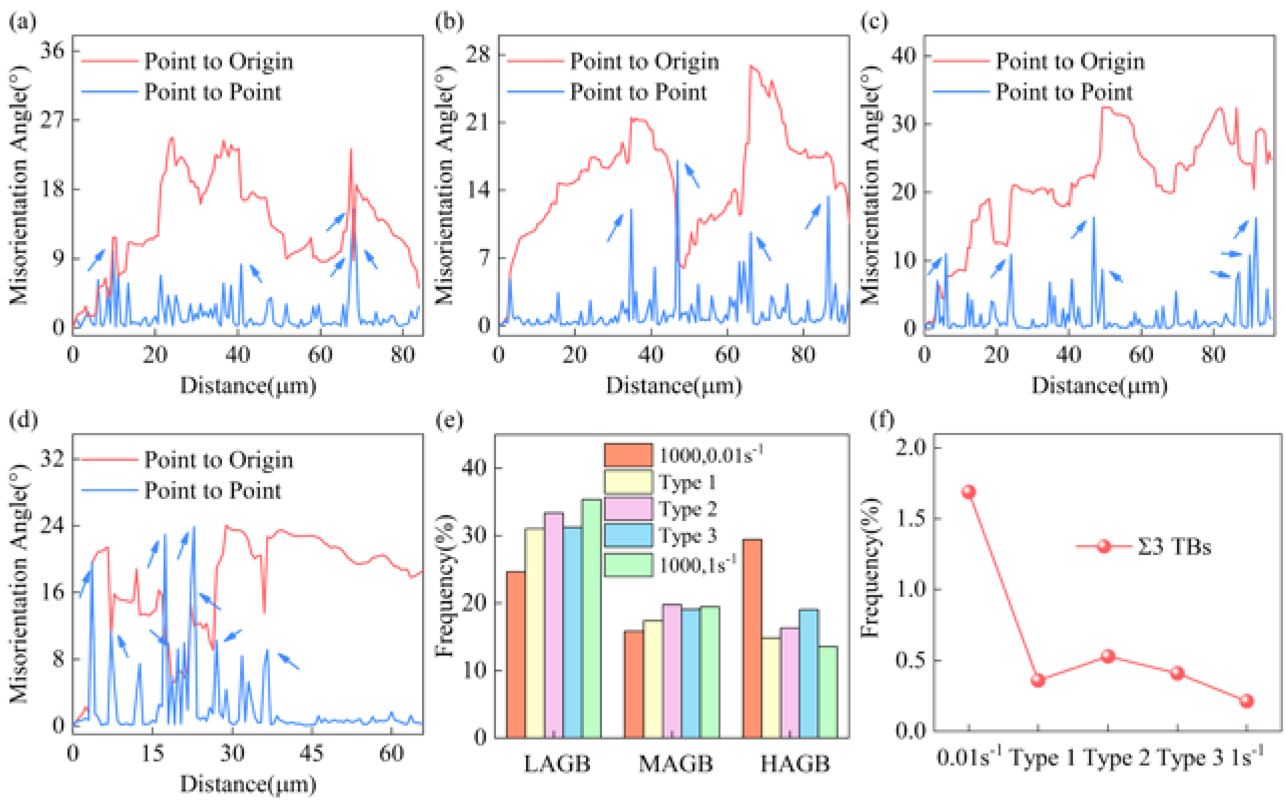

Fig. 22. The statistical information of the local (point to point) and cumulative (point to origin) misorientation angle

along the L1-L4 lines shown in Fig. 20 and the frequency of the boundaries with different misorientation angle at 1000℃ and a continuous increase in strain rate from $0.01s^{-1}$ to $1s^{-1}$ with different changing conditions: (a) Along the L1 line; (b)Along the L2 line; (c) Along the L3 line; (d) Along the L4 line; (e) The frequency of the LAGBs, MAGBs, and HAGBs at 0.9 true strain; (f) The frequency of the Σ3 TBs at 0.9 true strain.

Fig. 22. (e) shows the proportions of the LAGBs, MAGBs, and HAGBs for 0.9 true strain at different deformation conditions. The proportion of the LAGBs, MAGBs, and HAGBs in the continuous strain rate increase cases is between the constant $0.01s^{-1}$ and $1 s^{-1}$ strain rate deformation condition. Fig. 22. (f) statistics on the proportion of the Σ3 TBs. The constant $0.01s^{-1}$ strain rate deformation condition has the highest proportion. The three cases with continuously increasing strain rates have a slightly higher proportion of the Σ3 TBs than the constant $1s^{-1}$ deformation condition. The formation of the DRX grains at low strain rates increases the proportion of the HAGBs and Σ3 TBs and decreases the proportion of the LAGBs and MAGBs. At high strain rates, there is almost no DRX grain formation, and the substructure is preserved [74,75]. The substructure is susceptible to transition to the HAGBs, and the DRX occurs. The variation in the proportions of the different type boundaries under the above deformation conditions is accompanied by the evolution of substructures and DRX structures.

Fig. 23. (a)-(f) shows the local average misorientation images for 0.6 and 0.9 true strain at the conditions mentioned above (type 1, 2, and 3). Some green refined grains can be seen distributed along the grain boundaries (circled by the white dashed lines). This is consistent with the formation of substructures within the DRX grains in Fig. 20. As the deformation proceeds to 0.9 true strain, the blue DRX grains are formed along the grain boundaries (circled by the yellow dashed lines). This is attributed to the reoccurrence of DRX phenomena. In addition, many low dislocation density regions wrapped by highly local misorientation boundaries (pointed out by the yellow arrows) are formed within the grains. Moreover, there are almost no microbands in deformed grains.

Overall, a certain degree of low strain rate deformation prior to high strain rate deformation is beneficial in improving hot workability. The low strain rate deformation results in the formation of substructural networks within the grains and a small number of DRX grains distributed along grain boundaries. These microstructures significantly improve the deformation mechanism at high strain rates. The substructural networks act as a trap for dislocations, which prevents dislocations from slipping in a fixed direction at high strain rates and improves the deformation ability. Moreover, the small amount of DRX grains distributed along the grain boundaries can coordinate deformation. It also serves as the location of nucleation to promote the DRX effect. The deformation energy is effectively consumed under the joint action, which improves the hot workability.

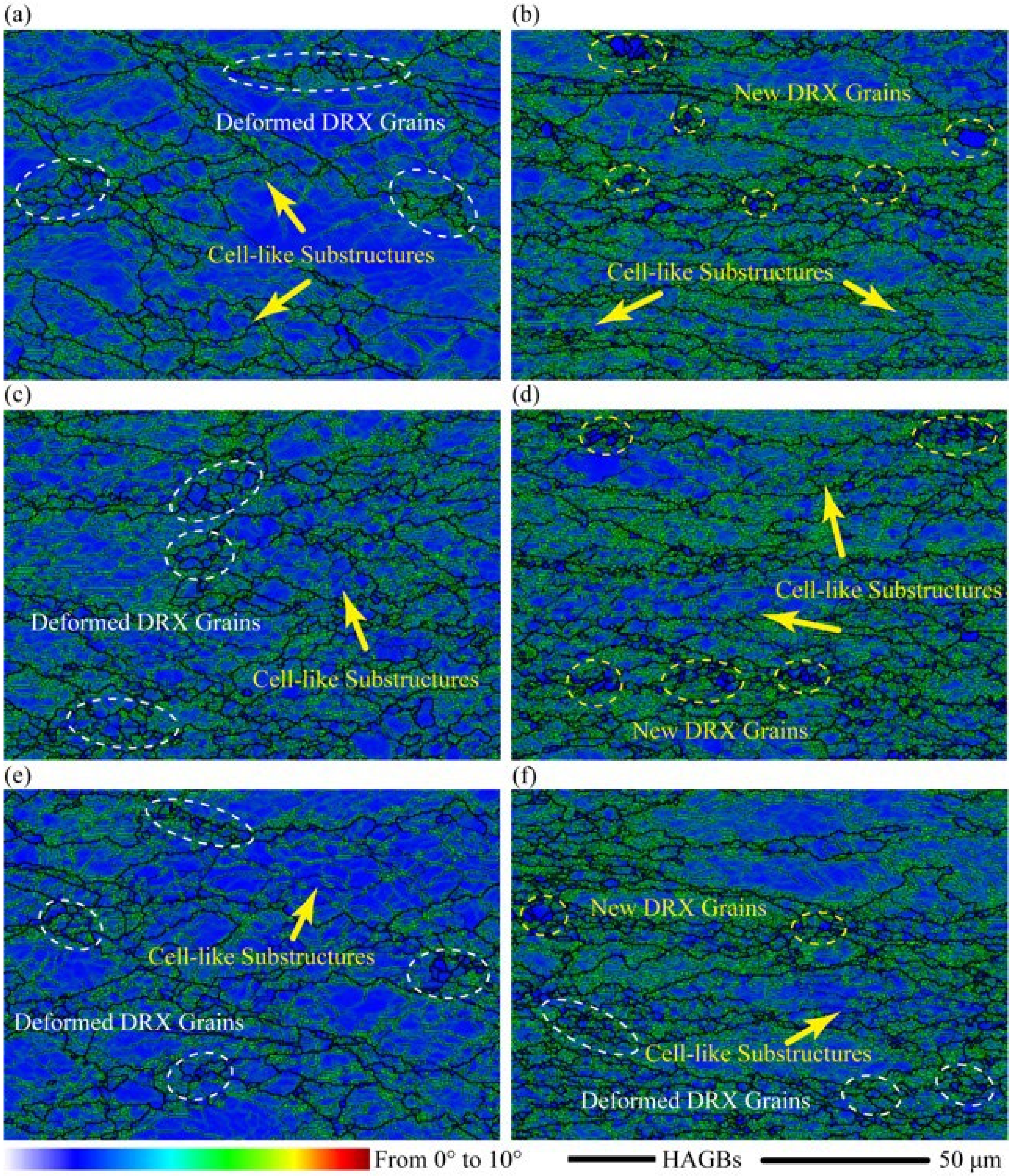

Fig. 23. The local average misorientation images at 1000°C and a continuous increase in strain rate from $0.01s^{-1}$ to $1s^{-1}$ with different changing conditions and deformation degree, where the black lines represent the HAGBs and the color from blue to red represent the values of the local average misorientation: (a) The image for the type 1 changing condition at 0.6 true strain; (b) The image for the type 1 changing condition at 0.9 true strain; (c) The image for the type 2 changing condition at 0.6 true strain; (d) The image for the type 2 changing condition at 0.9 true strain; (e)

The image for the type 3 changing condition at 0.6 true strain; (f) The image for the type 3 changing condition at 0.9 true strain.

4.2.2 Under the strain rate continuous decrease deformation conditions

Fig. 24. (a)-(d) shows the flow stress, DRX fraction, normalized dislocation density, and AGS curves under the deformation state of strain rate continuous decrease. The black dashed lines show the results under steady-state deformation conditions. The colored solid lines are the predicted results. The dots are the corresponding experimental values. The deformation temperature is 1000 °C. Firstly, the sample is deformed to 0.4 true strain at 1 s^{-1}, followed by a decrease of the strain rate to 0.01 s^{-1} during successive deformations. Table. 1. demonstrates the experimental conditions. In the type 4 condition, the strain rate undergoes a transient decrease. In the type 5 condition, the strain rate completes the decrease at 0.6 true strain. In the type 6 condition, the strain rate completes the decrease at 0.9 true strain. Accompanied by the decrease in strain rate, the flow stress decreases rapidly and gradually approaches a steady state. The decrease in flow stress is attributed to the direct effect of the change in deformation conditions and the promoted dynamic softening [76, 77]. In Fig. 24. (c), the dislocation density decreases rapidly under the effect of DRV and DRX [78, 79]. Accompanied by rapidly occurring DRX, the grains are refined. Fig. 24. (e)-(f) shows the changes of η and ξ. When a continuous decrease in strain rate occurs, the η increases significantly, and the ξ becomes positive. The continuous reduction of strain rate during deformation is favourable to improving the hot workability [80, 81].

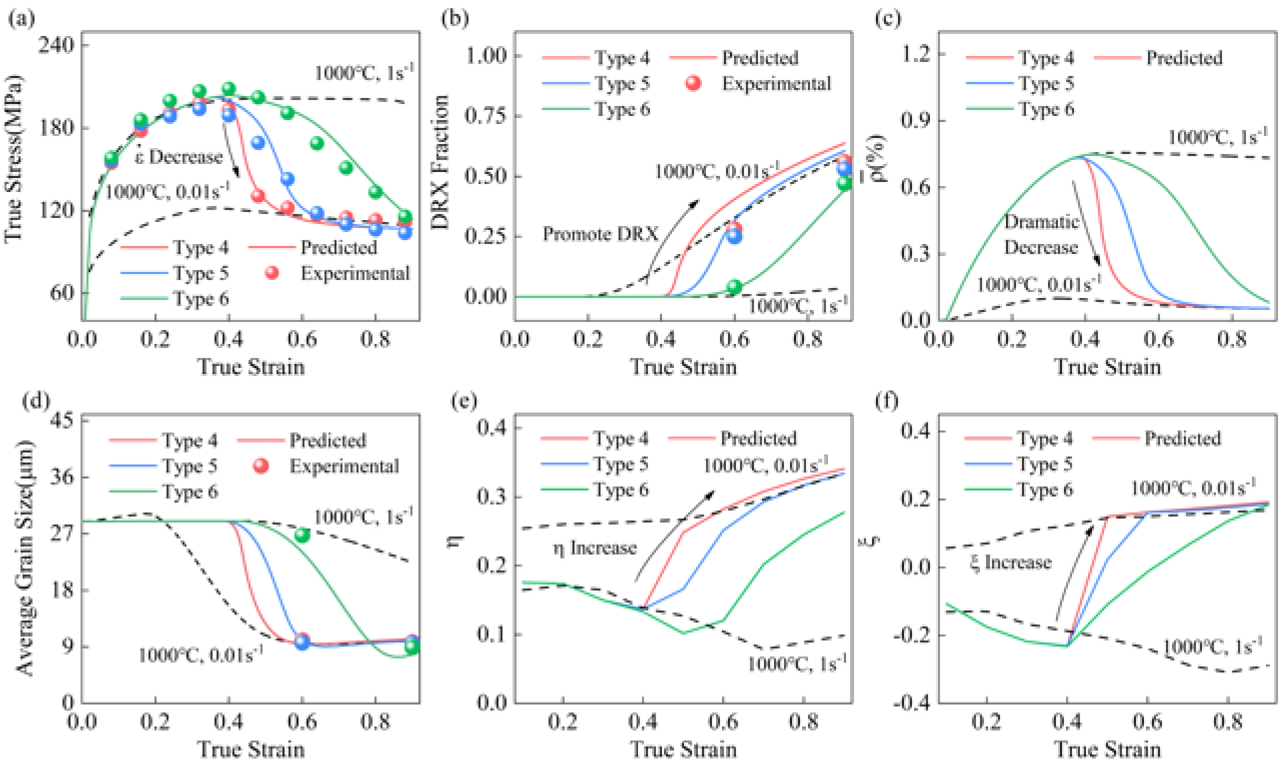

Fig. 24. The predicted flow stress, DRX fraction, normalized dislocation density, AGS, hot workability, and the corresponding experimental data at 1000°C and a continuous decrease in strain rate from $1s^{-1}$ to $0.01s^{-1}$, where the solid lines are the predicted values, the solid dots are the experimental values and the colors represent different conditions of strain rate changing shown in Table. 1: (a) The flow stress evolution; (b) The DRX fraction evolution; (c) The Normalized dislocation density evolution; (d) The AGS evolution; (e) The η evolution; (f) The ξ evolution.

Fig. 25. (a)-(f) shows the superposition of the band contrast and the grain boundary images for 0.6 and 0.9 true strain at the conditions mentioned above (type 4, 5, and 6). Microbands remain inside the grains (pointed out by the white arrows). Moreover, the substructure networks are developed from the microbands (pointed out by the pink arrows). As the deformation proceeds, many DRX grains with the Σ3 TBs are formed, indicating the grain boundaries' long-range migration. The deformation with a high strain rate generates a large amount of dislocation. The reduced strain rate provides sufficient time for the grain boundary migration, promoting the DRX process [82, 83]. In addition, the microbands undergo further interactions at low strain rates. This leads to the decomposition of the band substructure and the formation of the substructure networks. Fig. 26. (a)-(d) show the local (point to point) and cumulative (point to origin) misorientation angle along the L1-L4 lines in Fig. 25. Fig. 26. (a)-(b) show the misorientation information of the substructure networks formed within the deformed grains. Some locations with local misorientation angles between 5° and 15° appear, indicating that the misorientation angle of the LAGBs and MABGs further increased. The cumulative misorientation gradually accumulates. In particular, the cumulative misorientation in the L1 direction even approaches 60°, indicating the significant development of the substructure. Fig. 26. (c)-(d) show the misorientation information of retained microbands. Repeated fluctuations in the cumulative misorientation are a typical microband structure feature. There are only a few locations where the local misorientation exceeds 5°, indicating disintegration of the microbands at low strain rates.

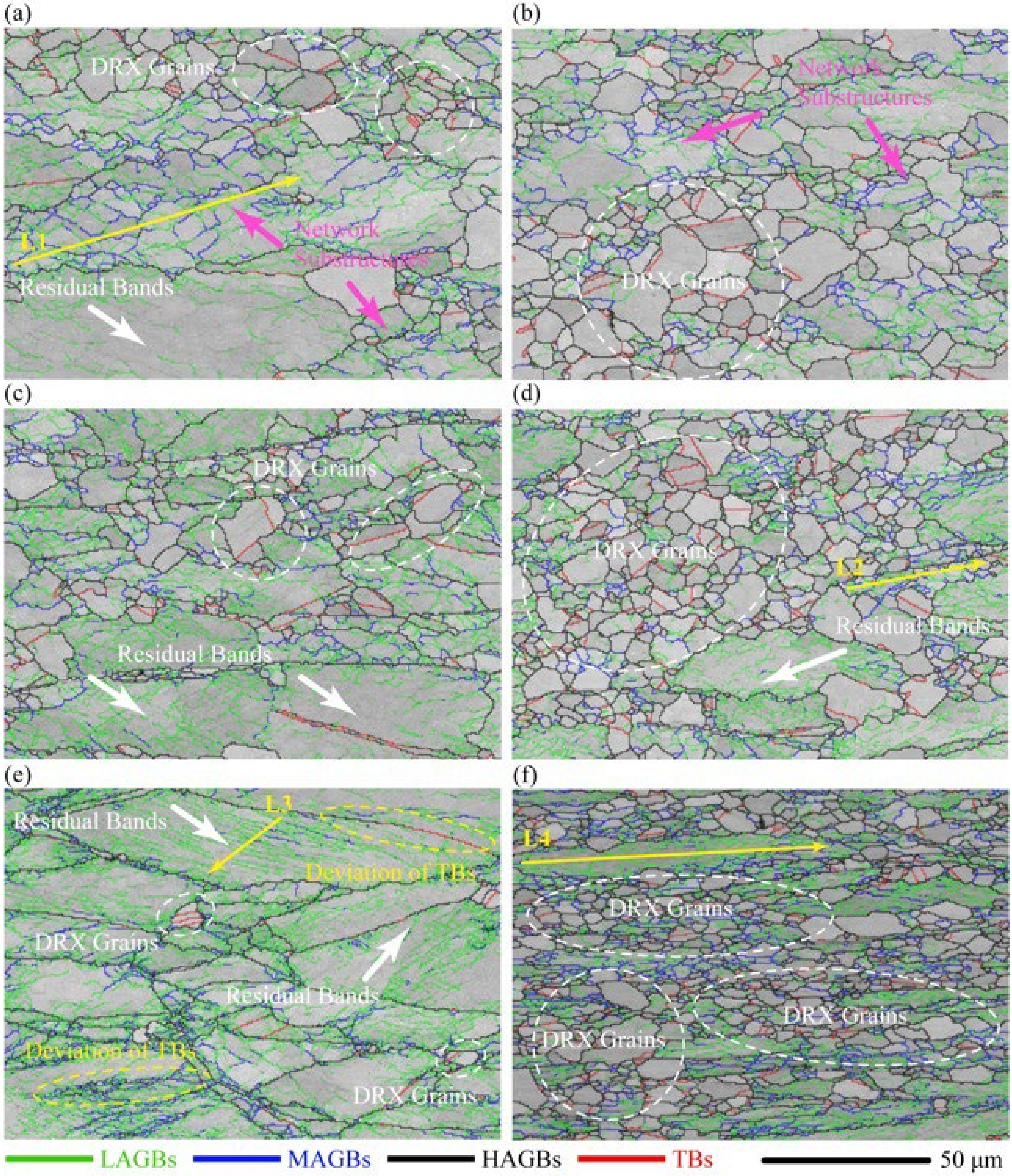

Fig. 25. The superposition of the band contrast and the grain boundary images at 1000°C and a continuous decrease in strain rate from $1s^{-1}$ to $0.01s^{-1}$ with different changing conditions and deformation degree, where the green lines represent the LAGBs, the blue lines represent the MAGBs, the black lines represent the HAGBs and the red lines represent the TBs: (a) The image for the type 1 changing condition at 0.6 true strain; (b) The image for the type 1 changing condition at 0.9 true strain; (c) The image for the type 2 changing condition at 0.6 true strain; (d) The

image for the type 2 changing condition at 0.9 true strain; (e) The image for the type 3 changing condition at 0.6 true strain; (f) The image for the type 3 changing condition at 0.9 true strain.

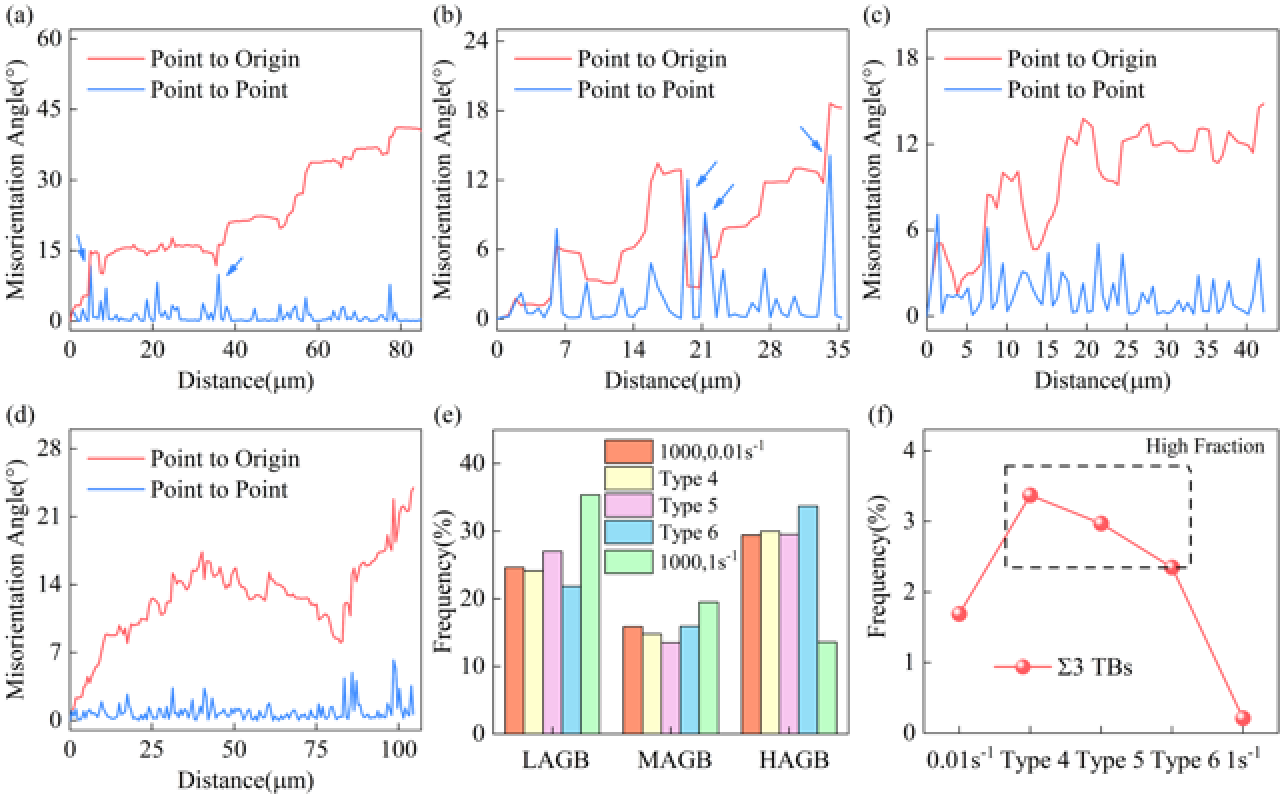

Fig. 26. The statistical information of the local and cumulative misorientation angle along the L1-L4 lines in Fig. 25 and the frequency of the boundaries with different misorientation angles at 1000°C and a continuous decrease in strain rate from $1s^{-1}$ to $0.01s^{-1}$ with different changing conditions: (a) Along the L1 line; (b)Along the L2 line; (c) Along the L3 line; (d) Along the L4 line; (e) The frequency of the LAGBs, MAGBs, and HAGBs at 0.9 true strain; (f) The frequency of the Σ3 TBs at 0.9 true strain.

Fig. 26. (e) shows the proportions of the LAGBs, MAGBs, and HAGBs for 0.9 true strain at deformation conditions. The continuous decrease of strain rate reduces the proportion of the LAGBs and MAGBs and increases the proportion of the HAGBs. Fig. 26. (f) statistics on the proportion of the Σ3 TBs. The continuous decrease in strain rate significantly increases the proportion of the Σ3 TBs. A large amount of dislocation density accumulated at a high strain rate enhances the grain boundaries migration ability [84, 85]. Fig. 27. (a)-(f) shows the local average misorientation images for 0.6 and 0.9 true strain at the conditions mentioned above (type 4, 5, and 6). The equiaxed grains with low dislocation density replace the deformed grains. Together, the above phenomena prove that DRX is promoted.

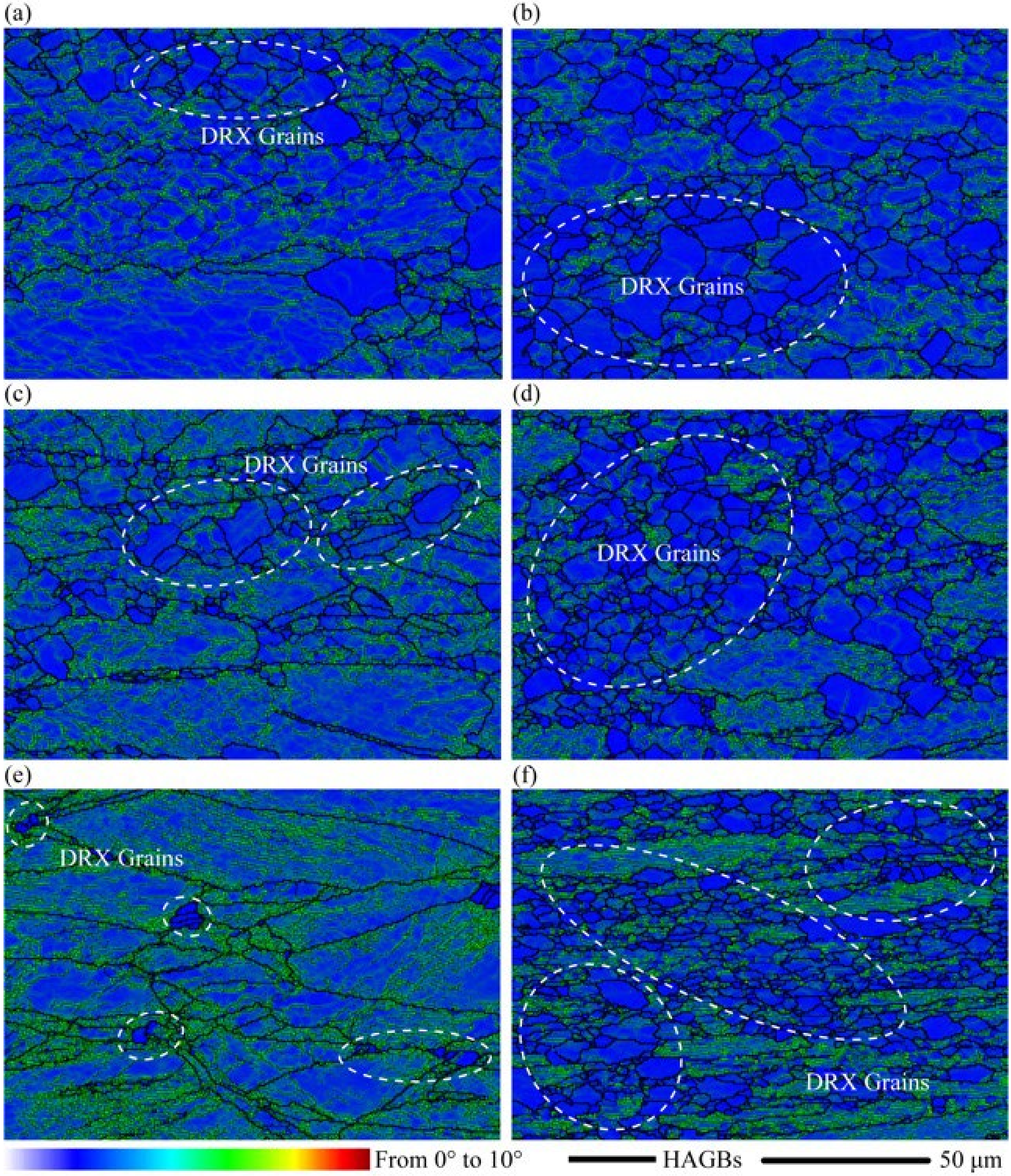

Fig. 27. The local average misorientation images at 1000℃ and a continuous decrease in strain rate from $1s^{-1}$ to $0.01s^{-1}$ with different changing conditions and deformation degree, where the black lines represent the HAGBs and the color from blue to red represent the values of local average misorientation: (a) The image for the type 4 changing condition at 0.6 true strain; (b) The image for the type 4 changing condition at 0.9 true strain; (c) The image for the type 5 changing condition at 0.6 true strain; (d) The image for the type 5 changing condition at 0.9 true strain; (e)

The image for the type 6 changing condition at 0.6 true strain; (f) The image for the type 6 changing condition at 0.9 true strain.

Overall, reducing the strain rate during deformation with a high strain rate improves hot workability. The low strain rate provides sufficient time to consume the deformation energy. Under DRV, the deformation bands are disintegrated and reorganized, forming a network substructure. The formation of excessive DRX grains consumes many dislocations. The significant softening effect improves the hot workability.

4.2.3 Summary of hot workability and corresponding microstructure evolution mechanisms

As shown in Fig. 28. (a), the hot workability under constant deformation conditions is divided into three regions. The microbands and macro shear deformation zones are formed under the high $\dot{\varepsilon}$ and low T. The deformation localization leads to a low η and negative ξ. Due to the suppression of dynamic softening, the efficiency of plastic deformation energy dissipation decreases continuously, deteriorating the hot workability [86,87]. Multiple DRX mechanisms co-occur at low $\dot{\varepsilon}$ and T and high $\dot{\varepsilon}$ and T. This region has a relatively high η and a positive ξ. DRX occurs quickly and saturates at high T and low $\dot{\varepsilon}$, leading to high η. However, the subsequent grain growth reduces the η. Excessive deformation should not be carried out at this condition to avoid the coarse grains.

Fig. 28. (b) shows the hot workability under non-constant deformation conditions. The initial low $\dot{\varepsilon}$ deformation forms a cell-like substructure network, and DDRX grains in the deformation state continuously increase the $\dot{\varepsilon}$. The cell-like substructure hinders the microband development after the $\dot{\varepsilon}$ continuously increases. The DDRX grains also share part of the deformation, forming internal LAGBs and MAGBs. This alleviates the deformation localization. Thus, the hot workability is improved compared to the high $\dot{\varepsilon}$ in constant deformation conditions. In the deformation state with the $\dot{\varepsilon}$ continuously decreasing, the initial high $\dot{\varepsilon}$ deformation leads to many dislocation densities and microbands with uneven distribution between grains. The subsequent decreasing $\dot{\varepsilon}$ deformation brings sufficient time to consume the initially accumulated deformation energy. The microbands decompose inside the grain. And some microbands form substructure networks. In addition, the inhomogeneity of the deformation energy storage between grains promotes the DDRX. Many DRX grains containing TBs appeared, effectively improving the hot workability.

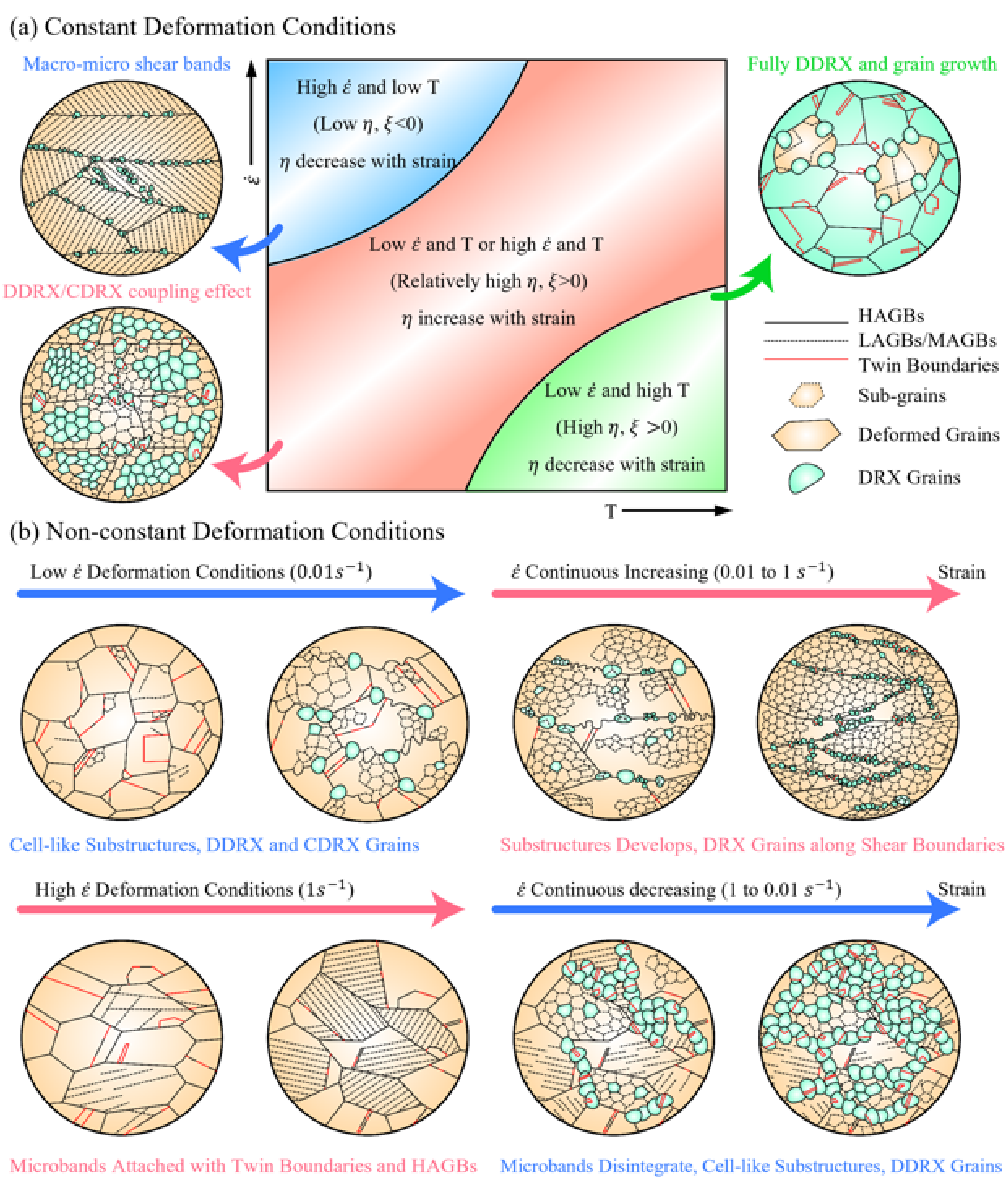

Fig. 28. Hot workability and corresponding microstructure evolution mechanism under: (a) different constant deformation conditions (temperature: 1000-1100°C and strain rate: 0.01-1 s^{-1}); (b) non-constant deformation conditions (temperature: 1000°C and strain rate continuous increase from 0.01 to 1 s^{-1} and decrease from 1 to 0.01 s^{-1}).

5.Conclusions

The main work of this paper is to establish a hot workability assessment method applicable to non-constant deformation conditions. The prediction method constructs a neural network model that takes the microstructure state and deformation conditions as input variables to obtain the power dissipation rate and deformation instability factor. Experimental data under constant deformation conditions train the relationship between input and output variables. The proposed method successfully predicts hot workability for constant and non-constant deformation conditions.

Moreover, combined with the model and characterization, the relationship between hot workability, microstructure states and deformation conditions under constant deformation conditions is analyzed. Hot workability is relevant to the mechanisms of microstructure evolution under the influence of deformation conditions. DRX is suppressed at high strain rates and low temperatures, and the dislocation density saturates rapidly. The formation of macro- and micro-deformation bands deteriorates the hot workability. The synergistic effect of DRX and DRV at low temperatures and strain rates continues improving hot workability. The rapid onset of DRX and subsequent grain growth at high temperatures and low strain rates limits hot workability.

Finally, the hot workability evolution mechanism under dynamic variation of deformation conditions is investigated. Appropriate deformation with a low strain rate prior to deformation with a high strain rate can improve hot workability. DRX behavior is promoted, and the deformation bands are suppressed. Reducing the strain rate during deformation with a high strain rate also improves hot workability. Sufficient DRX and DRV consume a large amount of accumulated deformation energy.

Acknowledgments

This work was supported by Regional Joint Funds of the National Natural Science Foundation of China (U20A20289); Innovative Talents International Cooperative Training Project of China Scholarship Council(CXXM20240010); The General Program of National Natural Science Foundation of China (52075471); Innovative Research Groups Project of the Natural Science Foundation of Hebei Province (E2021203011); Youth Fund of the Natural Science Foundation of Hebei Province (E2023203007); Innovative Capacity Cultivation Funding Project for Postgraduates of Hebei Province (CXZZSS2023040).

Reference

[1] Sakai T, Belyakov A, Kaibyshev R, Miura H, Jonas JJ. Dynamic and post-dynamic recrystallization under hot, cold and severe plastic deformation conditions. Progress in Materials Science 2014;60:130–207. https://doi.org/10.1016/j.pmatsci.2013.09.002.

[2] Huang K, Logé RE. A review of dynamic recrystallization phenomena in metallic materials. Materials &

Design 2016;111:548–74. https://doi.org/10.1016/j.matdes.2016.09.012.

[3] Aghajani Derazkola H, Garcia E, Murillo-Marrodán A, Conde Fernandez A. Review on modeling and simulation of dynamic recrystallization of martensitic stainless steels during bulk hot deformation. Journal of Materials Research and Technology 2022;18:2993–3025. https://doi.org/10/gqc8th.

[4] Bembalge OB, Panigrahi SK. Hot deformation behavior and processing map development of cryorolled AA6063 alloy under compression and tension. International Journal of Mechanical Sciences 2021;191:106100. https://doi.org/10.1016/j.ijmecsci.2020.106100.

[5] Malik A, Wang Y, Huanwu C, Nazeer F, Ahmed B, Khan MA, et al. Constitutive analysis, twinning, recrystallization, and crack in fine-grained ZK61 Mg alloy during high strain rate compression over a wide range of temperatures. Materials Science and Engineering: A 2020;771:138649. https://doi.org/10.1016/j.msea.2019.138649.

[6] Zhao M, Huang L, Li C, Li J, Li P. Evaluation of the deformation behaviors and hot workability of a high-strength low-alloy steel. Materials Science and Engineering: A 2021;810:141031. https://doi.org/10/gkpj9m.

[7] Long J, Xia Q, Xiao G, Qin Y, Yuan S. Flow characterization of magnesium alloy ZK61 during hot deformation with improved constitutive equations and using activation energy maps. International Journal of Mechanical Sciences 2021;191:106069. https://doi.org/10.1016/j.ijmecsci.2020.106069.

[8] Ding X, Zhao F, Shuang Y, Ma L, Chu Z, Zhao C. Characterization of hot deformation behavior of as-extruded AZ31 alloy through kinetic analysis and processing maps. Journal of Materials Processing Technology 2020;276:116325. https://doi.org/10.1016/j.jmatprotec.2019.116325.

[9] Singh G, Nayan N, Narayana Murty SVS, Yadava M, Bajargan G, Mohan M. Hot deformation behavior of Sc/Nb modified AA2195 Al–Li–Cu alloys. Materials Science and Engineering: A 2022;844:143169. https://doi.org/10.1016/j.msea.2022.143169.

[10] Wang H, Zhang H, Liu C, Ruan J, Huang H, Zhou X, et al. Hot deformation behavior, superplasticity and microstructure evolution of a new hot isostatic pressed nickel-based superalloy. Materials Science and Engineering: A 2024;891:145997. https://doi.org/10.1016/j.msea.2023.145997.

[11] Zhao Q, Yang F, Torrens R, Bolzoni L. Comparison of hot deformation behaviour and microstructural evolution for Ti-5Al-5V-5Mo-3Cr alloys prepared by powder metallurgy and ingot metallurgy approaches. Materials & Design 2019;169:107682. https://doi.org/10.1016/j.matdes.2019.107682.

[12] Nayan N, Singh G, Souza PM, Murty SVSN, Venkatesh M, Shivram BRNV, et al. Hot workability and microstructure control in Monel®400 (Ni–30Cu) alloy: An approach using processing map, constitutive equation and deformation modeling. Materials Science and Engineering: A 2021;825:141855.

https://doi.org/10.1016/j.msea.2021.141855.

[13] Rajput SK, Chaudhari GP, Nath SK. Characterization of hot deformation behavior of a low carbon steel using processing maps, constitutive equations and Zener-Hollomon parameter. Journal of Materials Processing Technology 2016;237:113–25. https://doi.org/10/gqg2wx.

[14] Peng Y, Guo S, Liu C, Barella S, Liang S, Gruttadauria A, et al. Dynamic recrystallization behavior of low-carbon steel during hot rolling process: modeling and simulation. Journal of Materials Research and Technology 2022;20:1266–90. https://doi.org/10.1016/j.jmrt.2022.07.039.

[15] Kim HY, Kwon HC, Lee HW, Im YT, Byon SM, Park HD. Processing map approach for surface defect prediction in the hot bar rolling. Journal of Materials Processing Technology 2008;205:70–80. https://doi.org/10/c98v4j.

[16] Sun Y, Feng X, Hu L, Zhang H, Zhang H. Characterization on hot deformation behavior of Ti-22Al-25Nb alloy using a combination of 3D processing maps and finite element simulation method. Journal of Alloys and Compounds 2018;753:256–71. https://doi.org/10/gdn6s4.

[17] Łukaszek-Sołek A, Krawczyk J, Śleboda T, Grelowski J. Optimization of the hot forging parameters for 4340 steel by processing maps. Journal of Materials Research and Technology 2019;8:3281 – 90. https://doi.org/10.1016/j.jmrt.2019.05.018.

[18] Lin C-N, Tzeng Y-C, Lee S-L, Fuh Y-K, Lukaszek-Solek A, Lin C-Y, et al. Optimization of hot deformation processing parameters for as-extruded 7005 alloys through the integration of 3D processing maps and FEM numerical simulation. JOURNAL OF ALLOYS AND COMPOUNDS 2023;948:169804. https://doi.org/10.1016/j.jallcom.2023.169804.

[19] Fuh Y-K, Shih J-K, Saputro IE, Chen C-P, Huang C-F, Ku H-Y, et al. Preform design with increased materials utilization and processing map analysis for aluminum hot forging process. Journal of Manufacturing Processes 2023;90:14–27. https://doi.org/10.1016/j.jmapro.2023.02.006.

[20] Jeong HY, Park J, Kim Y, Shin SY, Kim N. Processing parameters optimization in hot forging of AISI 4340 steel using instability map and reinforcement learning. Journal of Materials Research and Technology 2023;23:1995–2009. https://doi.org/10.1016/j.jmrt.2023.01.106.

[21] Hu X, Wang Z, Wang L, Chen C, Zhang F, Zhang W. Effect of pre-deformation on hot workability of super austenitic stainless steel. Journal of Materials Research and Technology 2022;16:238–50. https://doi.org/10.1016/j.jmrt.2021.11.163.

[22] Wu Z, Tang Y, Chen W, Lu L, Li E, Li Z, et al. Exploring the influence of Al content on the hot deformation

behavior of FeMn-Al-C steels through 3D processing map. VACUUM 2019;159:447–55. https://doi.org/10.1016/j.vacuum.2018.10.079.

[23] Pierce DT, Field DM, Limmer KR, Muth T, Sebeck KM. Hot deformation behavior of an industrially cast large grained low density austenitic steel. Materials Science and Engineering: A 2021;825:141785. https://doi.org/10.1016/j.msea.2021.141785.

[24] Nie X, Dong S, Wang F, Jin L, Zhang Z, Dong J, et al. Flow behavior and formability of hot-rolled Mg-8Gd-3Y alloy under double-pass isothermal compression. Journal of Materials Processing Technology 2020;275:116328. https://doi.org/10.1016/j.jmatprotec.2019.116328.

[25] Chen W, Hu B, Jia C, Zheng C, Li D. Continuous dynamic recrystallization during the transient deformation in a Ni-30%Fe austenitic model alloy. Materials Science and Engineering: A 2019;751:10–4. https://doi.org/10.1016/j.msea.2019.02.048.

[26] Liu C, Barella S, Peng Y, Guo S, Liang S, Sun J, et al. Modeling and characterization of dynamic recrystallization under variable deformation states. International Journal of Mechanical Sciences 2023:238:107838. https://doi.org/10.1016/j.ijmecsci.2022.107838.

[27] Wang M, Sun C, Fu MW, Liu Z, Wang C. Microstructure and microtexture evolution of dynamic recrystallization during hot deformation of a nickel-based superalloy. Materials & Design 2020;188:108429. https://doi.org/10.1016/j.matdes.2019.108429.

[28] Wu Y, Wang D, Liu Z, Liu G. A unified internal state variable material model for Ti2AlNb-alloy and its applications in hot gas forming. International Journal of Mechanical Sciences 2019;164:105126. https://doi.org/10.1016/j.ijmecsci.2019.105126.

[29] Chen X-M, Ning M-T, Hu H-W, Lin Y-C, Zhou X-J, Zhang J, et al. Investigation on microstructural and microhardness evolution of GH4698 superalloy under transiently varying strain rates. Materials Science and Engineering: A 2024;892:146014. https://doi.org/10.1016/j.msea.2023.146014.

[30] Samantaray D, Mandal S, Jayalakshmi M, Athreya CN, Bhaduri AK, Subramanya Sarma V. New insights into the relationship between dynamic softening phenomena and efficiency of hot working domains of a nitrogen enhanced 316L(N) stainless steel. Materials Science and Engineering: A 2014;598:368–75. https://doi.org/10.1016/j.msea.2013.12.105.

[31] Li C, Huang L, Zhao M, Zhang X, Li J, Li P. Influence of hot deformation on dynamic recrystallization behavior of 300M steel: Rules and modeling. Materials Science and Engineering: A 2020;797:139925. https://doi.org/10.1016/j.msea.2020.139925.

[32] Lu S, Xin L, Wang K, Dong X, Fu M. High temperature deformation behavior and optimization of hot compression process parameters in TC11 titanium alloy with coarse lamellar original microstructure. Transactions of Nonferrous Metals Society of China 2013;23:353-360. https://doi.org/10.1016/S1003-6326(13)62469-3.

[33] Lin YC, Chen X-M. A critical review of experimental results and constitutive descriptions for metals and alloys in hot working. Materials & Design 2011;32:1733–59. https://doi.org/10/cbmbjp.

[34] Chen W, Li S, Bhandari KS, Aziz S, Chen X, Jung DW. Genetic optimized Al–Mg alloy constitutive modeling and activation energy analysis. International Journal of Mechanical Sciences 2023;244:108077. https://doi.org/10.1016/j.ijmecsci.2022.108077.

[35] Kumar S, Pradhan H, Shah N, Rahul M R, Phanikumar G. Machine learning enabled processing map generation for high-entropy alloy. Scripta Materialia 2023;234:115543. https://doi.org/10.1016/j.scriptamat.2023.115543.

[36] Wen D, Yue T, Xiong Y, Wang K, Wang J, Zheng Z, et al. High-temperature tensile characteristics and constitutive models of ultrahigh strength steel. Materials Science and Engineering: A 2021;803:140491. https://doi.org/10.1016/j.msea.2020.140491.

[37] Wen H, Jin J, Tang X, Wang X, Yang H, Zhang Y, et al. Machine learning-assisted constitutive modeling of a novel powder metallurgy superalloy. International Journal of Mechanical Sciences 2023:260:108654. https://doi.org/10.1016/j.ijmecsci.2023.108654.

[38] Wessel A, Morand L, Butz A, Helm D, Volk W. Machine learning-based sampling of virtual experiments within the full stress state. International Journal of Mechanical Sciences 2024;275:109307. https://doi.org/10.1016/j.ijmecsci.2024.109307.

[39] Li Y, Li S. Deep learning based phase transformation model for the prediction of microstructure and mechanical properties of hot-stamped parts. International Journal of Mechanical Sciences 2022;220:107134. https://doi.org/10.1016/j.ijmecsci.2022.107134.

[40] Liu C, Barella S, Peng Y, Sun J, Guo S, Liang S, et al. Dynamic recrystallization behavior under steady and transient mutation deformation state. Materials Science and Engineering: A 2022:143138. https://doi.org/10/gp24xn.

[41] Su Z, Sun C, Wang M, Qian L, Li X. Modeling of microstructure evolution of AZ80 magnesium alloy during hot working process using a unified internal state variable method. Journal of Magnesium and Alloys 2022;10:281–94. https://doi.org/10/gqp72x.

[42] Sun ZC, Wu HL, Cao J, Yin ZK. Modeling of continuous dynamic recrystallization of Al-Zn-Cu-Mg alloy during hot deformation based on the internal-state-variable (ISV) method. International Journal of Plasticity

2018;106:73–87. https://doi.org/10.1016/j.ijplas.2018.03.002.

[43] Wang M, Sun C, Fu M W, Liu Z, Wang C. Experimental investigations and constitutive modeling of the dynamic recrystallization behavior of Inconel 740 superalloy. Materials Science and Engineering: A 2020;793,139939. https://doi.org/10.1016/j.msea.2020.139939

[44] Xiao Y-W, Lin YC, Jiang Y-Q, Zhang X-Y, Pang G-D, Wang D, et al. A dislocation density-based model and processing maps of Ti-55511 alloy with bimodal microstructures during hot compression in α+β region. Materials Science and Engineering: A 2020;790:139692. https://doi.org/10.1016/j.msea.2020.139692.

[45] Liu C, Guo S, Liang S, Li R, Barella S, Peng Y, et al. Constitutive description of work hardening and dynamic softening behavior under variable deformation states. Journal of Materials Processing Technology 2023;322:118188. https://doi.org/10.1016/j.jmatprotec.2023.118188.

[46] Chen L, Luo R, Hou X, Yang Y, Sun J, Liu T, et al. Shear-compression flow behavior and thermoforming properties of GH4169 superalloy. Journal of Materials Processing Technology 2022;308:117728. https://doi.org/10.1016/j.jmatprotec.2022.117728.

[47] Zhu Y, Cao Y, Liu C, Luo R, Li N, Shu G, et al. Dynamic behavior and modified artificial neural network model for predicting flow stress during hot deformation of Alloy 925. Materials Today Communications 2020;25:101329. https://doi.org/10.1016/j.mtcomm.2020.101329.

[48] Xue D, Wei W, Shi W, Zhou X, Rong L, Wen S, et al. Microstructural evolution and constitutive analysis of Al-Mg-Zn-Er-Zr based on arrhenius-type and machine-learning algorithm. Materials Today Communications 2022;32:104076. https://doi.org/10.1016/j.mtcomm.2022.104076.

[49] Tang X, Wang B, Huo Y, Ma W, Zhou J, Ji H, et al. Unified modeling of flow behavior and microstructure evolution in hot forming of a Ni-based superalloy. Materials Science and Engineering: A 2016;662:54–64. https://doi.org/10.1016/j.msea.2016.03.044.

[50] Liu C, Peng Y, Barella S, Mapelli C, Liang S. Characterization of dynamic recrystallization behavior of low carbon steel under flexible rolling process. Materials Today Communications 2021;29:102777. https://doi.org/10/gp24ws.

[51] Peng Y, Liang S, Liu C, Barella S, Guo S, Gruttadauria A, et al. Dynamic Recrystallization Behavior Under Inhomogeneous Thermomechanical Deformation State. Steel Research Int 2022:2200574. https://doi.org/10.1002/srin.202200574.

[52] Xu W, Yuan C, Wu H, Yang Z, Yang G, Shan D, et al. Modeling of flow behavior and microstructure evolution for Mg-6Gd-5Y-0.3Zr alloy during hot deformation using a unified internal state variable method. Journal

of Materials Research and Technology 2020;9:7669–85. https://doi.org/10.1016/j.jmrt.2020.04.099.

[53] Zhong X, Wang L, Huang L, Liu F. Transition of dynamic recrystallization mechanism during hot deformation of Incoloy 028 alloy. Journal of Materials Science & Technology 2020;42:241–53. https://doi.org/10.1016/j.jmst.2019.08.058.

[54] Mizadeh H, Najafizadeh A. Extrapolation of flow curves at hot working conditions. Materials Science and Engineering: A 2009;527:1856–1860. https:// doi.org/10.1016/j.msea.2009.11.013.

[55] Chen X-M, Ning M-T, Hu H-W, Lin Y-C, Zhou X-J, Zhang J, et al. Characterization of hot deformation behavior and optimization of hot workability for GH4698 superalloy. Materials Characterization 2023;201:112916. https://doi.org/10.1016/j.matchar.2023.112916.

[56] Chi Z, Ren S, Qiao J, Qu J, Yang C, Xie Z, et al. Failure behaviors and processing maps with failure domains for hot compression of a powder metallurgy Ni-based superalloy. Journal of Materials Research and Technology 2022;20:3860–74. https://doi.org/10.1016/j.jmrt.2022.08.128.

[57] Beladi H, Cizek P, Hodgson PD. On the characteristics of substructure development through dynamic recrystallization. Acta Materialia 2010;58:3531–41. https://doi.org/10.1016/j.actamat.2010.02.026.

[58] Shen YF, Jia N, Misra RDK, Zuo L. Softening behavior by excessive twinning and adiabatic heating at high strain rate in a Fe–20Mn–0.6C TWIP steel. Acta Materialia 2016;103:229–42. https://doi.org/10/gqmx9n.

[59] Yu H, Wang Z, Ning Y, Huang S, Liu Q. DRX mechanisms of a Ni-Co-W type superalloy with typical columnar grains during hot compression. Journal of Alloys and Compounds 2023;959:170533. https://doi.org/10.1016/j.jallcom.2023.170533.

[60] Li M, Shi Z-Z, Wang Q, Cheng Y, Wang L-N. Zn–0.8Mn alloy for degradable structural applications: Hot compression behaviors, four dynamic recrystallization mechanisms, and better elevated-temperature strength. Journal of Materials Science & Technology 2023;137:159–75. https://doi.org/10.1016/j.jmst.2022.08.002.

[61] Ba LZ, Di XJ, Li CN, Qu YT, Pan J, Ma C, et al. Hot deformation behavior of a cryogenic high manganese steel based on the microstructure and texture evolution. Materials Characterization 2023;195:112554. https://doi.org/10.1016/j.matchar.2022.112554.

[62] Xie B, Li H, Ning Y, Fu M. Discontinuous dynamic recrystallization and nucleation mechanisms associated with 2-, 3- and 4-grain junctions of polycrystalline nickel-based superalloys. Materials & Design 2023;231:112041. https://doi.org/10.1016/j.matdes.2023.112041.

[63] Chen W, Jia C, Hu B, Zheng C, Li D. Evolution of twins and sub-boundaries at the early stage of dynamic recrystallization in a Ni-30%Fe austenitic model alloy. Materials Science and Engineering: A 2018;733:419–28.

https://doi.org/10.1016/j.msea.2018.07.071.

[64] Yanushkevich Z, Belyakov A, Kaibyshev R. Microstructural evolution of a 304-type austenitic stainless steel during rolling at temperatures of 773–1273 K. Acta Materialia 2015;82:244–54. https://doi.org/10.1016/j.actamat.2014.09.023.

[65] Chen L, Ding H, Liu T, Luo R, Cao Y, Zhang Y, et al. Thermal deformation behavior and microstructure evolution of GH4169 superalloy under the shear-compression deformation conditions. Materials & Design 2021;212:110195. https://doi.org/10.1016/j.matdes.2021.110195.

[66] Lin YC, Wu X-Y, Chen X-M, Chen J, Wen D-X, Zhang J-L, et al. EBSD study of a hot deformed nickel-based superalloy. Journal of Alloys and Compounds 2015;640:101–13. https://doi.org/10.1016/j.jallcom.2015.04.008.

[67] Marandi A, Zarei-Hanzaki R, Zarei-Hanzaki A, Abedi HR. Dynamic recrystallization behavior of new transformation–twinning induced plasticity steel. Materials Science and Engineering: A 2014;607:397–408. https://doi.org/10.1016/j.msea.2014.03.112.

[68] Buzolin RH, Lasnik M, Krumphals A, Poletti MC. A dislocation-based model for the microstructure evolution and the flow stress of a Ti5553 alloy. International Journal of Plasticity 2021;136:102862. https://doi.org/10.1016/j.ijplas.2020.102862.

[69] Zeng R, Huang L, Li J, Li H, Zhu H, Zhang X. Quantification of multiple softening processes occurring during multi-stage thermoforming of high-strength steel. International Journal of Plasticity 2019;120:64–87. https://doi.org/10.1016/j.ijplas.2019.04.010.

[70] Li Y, Gu B, Jiang S, Liu Y, Shi Z, Lin J. A CDRX-based material model for hot deformation of aluminium alloys. International Journal of Plasticity 2020;134:102844. https://doi.org/10.1016/j.ijplas.2020.102844.

[71] Takaki T, Yoshimoto C, Yamanaka A, Tomita Y. Multiscale modeling of hot-working with dynamic recrystallization by coupling microstructure evolution and macroscopic mechanical behavior. International Journal of Plasticity 2014;52:105–16. https://doi.org/10.1016/j.ijplas.2013.09.001.

[72] Cao T-S, Bobadilla C, Montmitonnet P, Bouchard P-O. A comparative study of three ductile damage approaches for fracture prediction in cold forming processes. Journal of Materials Processing Technology 2015;216:385–404. https://doi.org/10/gqn9fj.

[73] Chaudhuri A, Behera AN, Sarkar A, Kapoor R, Ray RK, Suwas S. Hot deformation behaviour of Mo-TZM and understanding the restoration processes involved. Acta Materialia 2019;164:153–64. https://doi.org/10.1016/j.actamat.2018.10.037.

[74] Chen W, Zheng C, Jia C, Hu B, Li D. Strain-rate dependence of the dynamic softening in a duplex stainless

steel. Materials Characterization 2020;162:110219. https://doi.org/10.1016/j.matchar.2020.110219.

[75] Hamedani H M, Tolaminejad B, Momeni A, Sadeghpour S. Hot deformation behavior and microstructural characterization of a novel high entropy steel. Materials Science and Engineering: A 2024;910:146884. https://doi.org/10.1016/j.msea.2024.146884.

[76] Li K-K, Chen M-S, Lin YC, Yuan W-Q. Microstructural evolution of an aged Ni-based superalloy under two-stage hot compression with different strain rates. Materials & Design 2016;111:344–52. https://doi.org/10.1016/j.matdes.2016.09.007.

[77] He D, Yan X-T, Lin YC, Zhang S, Chen Z-J. Microstructure evolution and constitutive model for a Ni-Mo-Cr base alloy in double-stages hot compression with step-strain rates. Materials Characterization 2022;194:112385. https://doi.org/10.1016/j.matchar.2022.112385.

[78] Kumar P, Nithin B, Samal S, Ghosh A. Hot deformation behavior and microstructural evolution of dual phase Ni48.6 Al10.3 Co17 Cr7.5 Fe9 Ti5.8 Ta0.6 Mo0.8 W0.4 high entropy alloy. Materials Science and Engineering: A 2024;910:146887. https://doi.org/10.1016/j.msea.2024.146887.

[79] Yao K J, Ren Q G, Zhao J, Wu Y M, Qin C, Dong J X, Zhang M C. Difference in hot deformation behavior of a Ni–Fe based superalloy through cast-wrought and additive manufactured processes. Materials Science and Engineering: A 2024;909:146869. https://doi.org/10.1016/j.msea.2024.146869.

[80] Miao J, Sutton S, Luo AA. Deformation microstructure and thermomechanical processing maps of homogenized AA2070 aluminum alloy. Materials Science and Engineering: A 2022;834:142619. https://doi.org/10.1016/j.msea.2022.142619.

[81] Chi Z, Ren S, Qiao J, Qu J, Yang C, Xie Z, et al. Failure behaviors and processing maps with failure domains for hot compression of a powder metallurgy Ni-based superalloy. Journal of Materials Research and Technology 2022;20:3860–74. https://doi.org/10.1016/j.jmrt.2022.08.128.

[82] Brown AA, Bammann DJ. Validation of a model for static and dynamic recrystallization in metals. International Journal of Plasticity 2012;32–33:17–35. https://doi.org/10.1016/j.ijplas.2011.12.006.

[83] Cai Y, Sun CY, Li YL, Hu SY, Zhu NY, Barker EI, et al. Phase field modeling of discontinuous dynamic recrystallization in hot deformation of magnesium alloys. International Journal of Plasticity 2020;133:102773. https://doi.org/10.1016/j.ijplas.2020.102773.

[84] Cizek P. The microstructure evolution and softening processes during high-temperature deformation of a 21Cr–10Ni–3Mo duplex stainless steel. Acta Materialia 2016;106:129–43. https://doi.org/10.1016/j.actamat.2016.01.012.

[85] Ba L Z, Li C N, Pan J, Ma C, Qu Y T, Yang X C, Di X J. Grain size dependence of hot deformation behaviors and resultant hot ductility in cryogenic high-manganese steel. Materials Science and Engineering: A 2024;899:146466. https://doi.org/10.1016/j.msea.2024.146466.

[86] Qiang D S, Sun M L, Wang F, Xie L C, Hua L, Dynamic recrystallization behaviors and cracking mechanism for the hot deformation of new-generation high nitrogen bearing steel. Materials & Design 2024;241:112891. https://doi.org/10.1016/j.matdes.2024.112891

[87] El Mehtedi M, Gabrielli F, Spigarelli S. Hot workability in process modeling of a bearing steel by using combined constitutive equations and dynamic material model. Materials & Design 2014;53:398–404. https://doi.org/10.1016/j.matdes.2013.07.055.